



An amphibious artificial vision system with a panoramic visual field

Mincheol Lee^{1,2,12}, Gil Ju Lee^{3,4,12}, Hyuk Jae Jang^{1,2}, Eehyung Joh^{1,2}, Hyojin Cho^{1,2}, Min Seok Kim^{1,2}, Hyun Myung Kim³, Kyeong Muk Kang³, Joong Hoon Lee³, Myunghbin Kim^{1,2}, Hongwoo Jang⁵, Ji-Eun Yeo³, Frédo Durand⁶, Nanshu Lu^{5,7,9,10,11}, Dae-Hyeong Kim^{1,2,8} and Young Min Song³✉

Biological visual systems have inspired the development of various artificial visual systems including those based on human eyes (terrestrial environment), insect eyes (terrestrial environment) and fish eyes (aquatic environment). However, attempts to develop systems for both terrestrial and aquatic environments remain limited, and bioinspired electronic eyes are restricted in their maximum field of view to a hemispherical field of view (around 180°). Here we report the development of an amphibious artificial vision system with a panoramic visual field inspired by the functional and anatomical structure of the compound eyes of a fiddler crab. We integrate a microlens array with a graded refractive index and a flexible comb-shaped silicon photodiode array on a spherical structure. The microlenses have a flat surface and maintain their focal length regardless of changes in the external refractive index between air and water. The comb-shaped image sensor arrays on the spherical substrate exhibit an extremely wide field of view covering almost the entire spherical geometry. We illustrate the capabilities of our system via optical simulations and imaging demonstrations in both air and water.

In nature, diverse vision systems with distinct imaging characteristics have evolved under different natural habitats. These have inspired the development of various artificial vision systems, including human-eye-type (terrestrial environment)^{1–4}, insect-eye-type (terrestrial environment)^{5,6} and fish-eye-type (aquatic environment)⁷ artificial vision. The fiddler crab (*Uca arcuata*), which lives in an intertidal region (both terrestrial and aquatic environment)⁸, has developed compound eyes with flat-face lenses that offer amphibious imaging capabilities and a panoramic visual field^{9,10}. The flat nature and graded refractive index (RI) of the corneal facet lens suppresses the defocusing effect caused by changes in the external environment¹⁰, and the structure of the compound eyes, which covers almost the entire eye stalk, enables an extremely wide field of view (FoV)⁹. Other crustaceans^{11,12} and insects¹³ living at the boundary between terrestrial and aquatic regions also have eyes with a flat corneal lens and a graded RI structure for amphibious imaging. These vision systems have inspired the development of artificial vision, but previous efforts to imitate the natural graded RI have focused on aberration correction¹³ and antireflection¹⁴. Furthermore, currently available bioinspired electronic eyes are limited in their maximum FoV to a hemispherical FoV (around 180°) and thus do not offer omnidirectional FoV (around 360°)^{3,5,7}.

In this Article, we report an amphibious artificial vision system with a panoramic FoV by mimicking the functional and anatomical structure of the fiddler crab eye. Microlens arrays with a flat surface and graded RI profile are integrated on flexible comb-shaped

silicon photodiode (Si PD) arrays, which are mounted on a three-dimensional (3D) spherical structure. The flat surface and graded RI profile of the microlens were optimized to have a consistent focusing power regardless of external RI changes. The integrated device exhibits an extremely wide FoV covering almost the entire 3D space. We illustrate the panoramic image acquisition capabilities of the integrated system under both air and water conditions. This approach to artificial vision could be used to develop imaging systems for panoramic motion detection and obstacle avoidance in variable environments.

Investigation of the anatomy of the fiddler crab eye

Some crabs that live in both terrestrial and aquatic environments have developed unique visual systems for amphibious and panoramic imaging^{15,16}. Specifically, semiterrestrial crabs (for example, fiddler crabs; Fig. 1a, centre)¹⁰ possess flattened corneas that enable amphibious imaging. Other types of crab, such as terrestrial^{16–20} and aquatic^{21–23} crabs (for example, vampire crabs and spanner crabs; Fig. 1a, left and right, respectively) that do not need amphibious imaging have curved corneas. Supplementary Table 1 provides more information about the ocular structures of crab families. Fiddler crabs have also evolved stalked eyes to enable omnidirectional viewing in both air and water (Fig. 1b). Thus, they can instantly avoid predators flying overhead (predator zone; Fig. 1c, red region) and detect conspecifics approaching their burrows⁸ (social zone; Fig. 1c, green region). The ellipsoidal structure of the fiddler crab eye provides it with a panoramic FoV (Fig. 1d). The distribution map of

¹Center for Nanoparticle Research, Institute for Basic Science (IBS), Seoul, Republic of Korea. ²School of Chemical and Biological Engineering, Institute of Chemical Processes, Seoul National University, Seoul, Republic of Korea. ³School of Electrical Engineering and Computer Science, Gwangju Institute of Science and Technology, Gwangju, Republic of Korea. ⁴Department of Electronics Engineering, Pusan National University, Busan, Republic of Korea. ⁵Texas Materials Institute, The University of Texas at Austin, Austin, TX, USA. ⁶Computer Science and Artificial Intelligence Laboratory, Massachusetts Institute of Technology, Cambridge, MA, USA. ⁷Department of Aerospace Engineering and Engineering Mechanics, The University of Texas at Austin, Austin, TX, USA. ⁸Department of Materials Science and Engineering, Seoul National University, Seoul, Republic of Korea. ⁹Department of Electrical and Computer Engineering, The University of Texas at Austin, Austin, TX, USA. ¹⁰Department of Biomedical Engineering, The University of Texas at Austin, Austin, TX, USA. ¹¹Department of Mechanical Engineering, The University of Texas at Austin, Austin, TX, USA. ¹²These authors contributed equally: Mincheol Lee, Gil Ju Lee, Hyuk Jae Jang. ✉e-mail: dkim98@snu.ac.kr; ymsong@gist.ac.kr

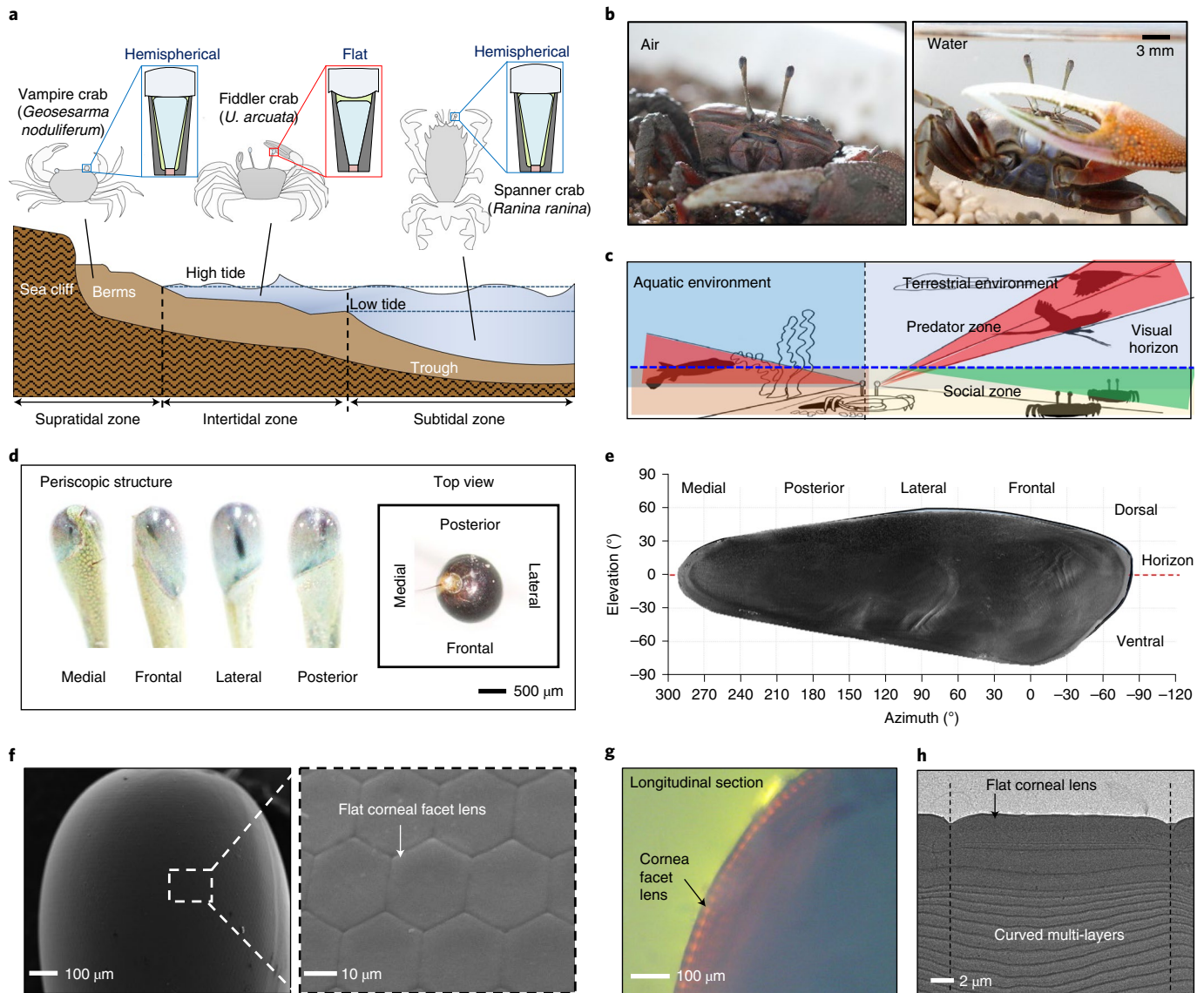


Fig. 1 | Structural characteristics of the fiddler crab eye. **a**, Crab families that inhabit neritic zones, and the ommatidium structure for each crab species. **b**, *Uca arcuata* in the terrestrial (left) and aquatic (right) environment. **c**, Visual ecology of the fiddler crab. **d**, Panoramic structure of a fiddler crab eye from the top view. **e**, Visual map reconstructed from the fiddler crab ommatidia. **f**, SEM image of the fiddler crab eye (left) and its magnified view (right). **g**, Optical microscopy image of the longitudinally sectioned fiddler crab eye. **h**, Cross-sectional TEM image of a single lens in an ommatidium of the fiddler crab eye.

the ommatidia in the fiddler crab eye shows their full wide angular coverage (360°) along the visual horizon (Fig. 1e)⁹.

Amphibious vision, which is associated with a flat corneal lens and graded RI structure in the ommatidia of the fiddler crab eye, exploits the panoramic visual advantages in both terrestrial and aquatic environments. To study the lens morphology, a fiddler crab eye was observed by scanning electron microscopy (SEM). The eye consists of thousands of ommatidia (Fig. 1f, left). The surface of the corneal facet lens in an ommatidium is flat (Fig. 1f, right). The lenses in the compound eyes of terrestrial arthropods, in contrast, have curved surfaces (Extended Data Fig. 1). An observation of the longitudinal section of the eye using optical microscopy confirmed that the lens has a smooth flat surface (Fig. 1g). This flat corneal lens experiences little change in the focusing power even when the external medium changes. Meanwhile, according to the cross-sectional observation of a single lens using transmission electron microscopy (TEM), a flat top surface and concavely curved multilayers are

observed (Fig. 1h). Such curved multilayers enable the focusing of incoming light onto photoreceptors (PRs) even though fiddler crabs have a flat corneal lens^{10,24}.

Characterization of the amphibious artificial ommatidium

Figure 2a displays important optical parts of a natural ommatidium of the fiddler crab, such as graded-index corneal lens (GCL), crystalline cone (CC) and screening pigment (SP). The SP blocks noisy light from adjacent ommatidia¹⁰. As shown in Fig. 1h, the concave multilayers are located under the flat GCL. In the natural world, however, there are two optical structures to implement the graded RI with a flat top surface: (1) the upper layers have a higher RI and the curvature of multilayers is concave¹¹ or (2) the upper layers have a lower RI and the curvature of multilayers is convex²⁵. Fig. 2b graphically summarizes the differences of these two structures. The concavely or convexly curved multilayers with graded RIs should have a negative radius of curvature (RoC) with descending RIs or a

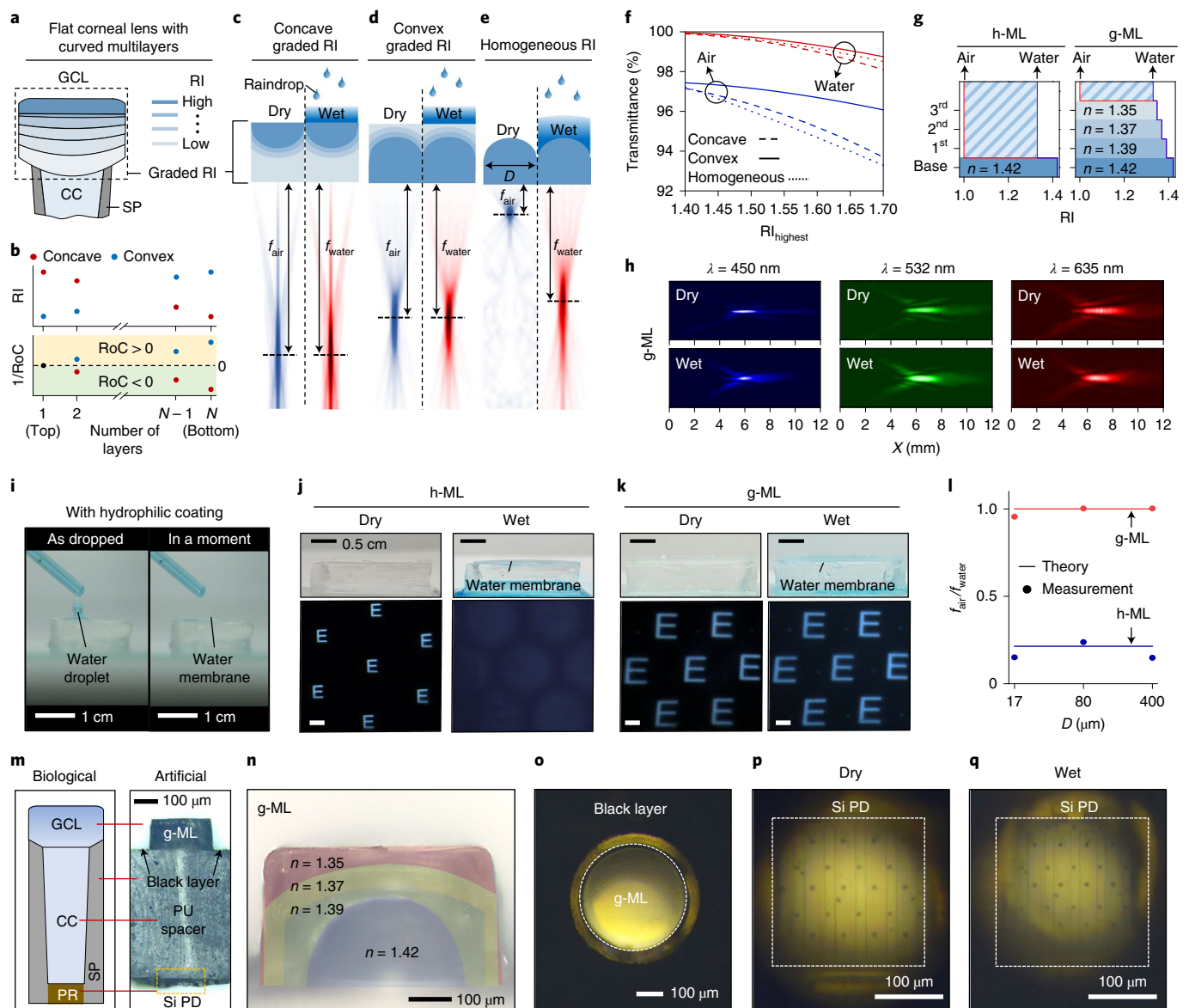


Fig. 2 | Optical simulation and experimental characterization of microlenses for amphibious imaging. **a**, Schematic of the natural ommatidium. **b**, RI and RoC changes in concavely and convexly curved multilayers for graded RI depending on the number of layers. **c–e**, Ray-tracing optical simulation results of the microlenses with the concave multilayers of graded RI (**c**), convex multilayers of graded RI (**d**) and typical microlens with a homogeneous RI (**e**) in the dry and wet state. **f**, Transmittance versus RI of the topmost layer in multilayered lenses with graded and homogeneous RIs. **g**, RI profile of h-ML (left) and g-ML (right). **h**, Measured light intensity distribution of g-ML for three wavelengths in air and water. **i**, Photographs to show instant conversion of a water droplet into a water membrane by the hydrophilic coating on g-ML. **j,k**, Imaging results by h-ML (**i**) and g-ML (**j**) ($D = 400 \mu\text{m}$) under the dry and wet condition. The coloured (sky blue) water membrane in the wet condition is shown on the microlens surface. **l**, Ratio of the focal length in air and water for g-ML and h-ML with various diameters. **m**, Comparison of the biological (left) and artificial (right) ommatidium. **n**, Magnified cross-sectional view of g-ML. The colourized layers show the graded interlayer structure and flat surface of g-ML. **o**, Photograph of the g-ML surface. **p,q**, Photographs of a photodiode taken through the g-ML in air (**p**) and water (**q**).

positive RoC with ascending RIs, respectively. The flat top surface is expressed as $1/\text{RoC} = 0$ because of an infinite RoC.

Ray-tracing simulations confirm that both types of multilayer exhibit amphibious focusing capabilities, which are evaluated by adding a layer of water to the surface of each lens (Fig. 2c,d). The graded RI lenses with flat top surfaces (that is, concave and convex graded RIs) maintained each identical focal length in air and water (that is, f_{air} and f_{water}), whereas a typical lens structure, which has no flat top surface, could not, which was attributed to the flat surface and graded RI (Fig. 2e). The typical lens corresponds to optical structures of a terrestrial arthropod eye (Extended Data Fig. 1),

and hence, terrestrial arthropod eyes lose their focusing power once they are in water. The RoC of the graded-index layers determines the focal length of the microlens with graded RI (Supplementary Fig. 1). The specifications of the simulated microlenses are listed in Supplementary Table 2.

Although both microlenses with concavely and convexly curved multilayers exhibit the amphibious feature, the convex gradient can be fabricated more easily than the concave gradient. Furthermore, graded RI multilayers with the convex curvature have an additional advantage, that is, the antireflection effect, which is helpful for the underwater condition with a weaker ambient light intensity than the

terrestrial region. The simulation result (Fig. 2f) demonstrates the antireflection effect of the convex RI gradient (that is, the highest transmittance for all the RI_{highest} values in air and water), whereas it is difficult to obtain the antireflection effect with a concave RI gradient owing to its structural limitation such as the highest RI at the top surface. Therefore, the convex curvature geometry was selected for the graded microlens (g-ML) with a flat surface. As a control group of g-ML, a typical lens structure with a homogeneous RI was used and called as a homogeneous microlens (h-ML). The RI values for the h-ML and g-ML are shown in Fig. 2g. The amphibious feature of the fabricated g-ML (diameter, $\sim 400\ \mu\text{m}$) was characterized in air and water at three wavelengths (for example, 450, 532 and 635 nm) (Fig. 2h). Identical focal lengths were obtained in air and water.

For all-weather imaging, a water droplet on the lenses should become a water membrane because a water droplet on the g-ML can cause the blurring of focal spots owing to the curvature of the water droplet. A hydrophilic coating using silica nanoparticles allows the instant conversion of the water droplet into a water membrane on the g-ML (Fig. 2i). Supplementary Fig. 2 shows the effect of a hydrophilic coating in more detail. With hydrophilic coatings, imaging demonstrations using g-MLs and h-MLs with diameters of $400\ \mu\text{m}$ confirmed the amphibious feature of the g-MLs (Fig. 2j,k). The g-MLs formed clear images (that is, the letter 'E') either with or without the water layer, whereas the h-MLs could not. The water layer on the h-ML surface changed the focal length, causing the images to become blurred. The focusing abilities of the g-ML and h-ML in air and water were compared at various scales (microlens diameters of 17, 80 and $400\ \mu\text{m}$) to confirm scale independence (Fig. 2l). Both theory and experiments indicated that the amphibious imaging ability of g-MLs is consistent regardless of the lens size. Extended Data Fig. 2 presents the detailed characterization results for the microlenses, and Extended Data Fig. 3 shows the experimental setup and other measurement results. Supplementary Note 1 provides the details of the experimental setup.

Figure 2m shows the cross section of a unit image sensing pixel with a g-ML (right), which mimics the geometry of a fiddler crab ommatidium (left). A unit pixel (that is, artificial ommatidium) consists of a flat g-ML, polyurethane (PU) elastomeric spacer and Si PD, which mimic the flat-facet lens, CC and PR of the fiddler crab ommatidium, respectively. A black layer coated around the lens blocks the stray light²⁶, as the SP does in the fiddler crab eye. The magnified cross-sectional view of the g-ML (Fig. 2n) shows that multilayered lenses with different RIs are stacked on the base lens. The g-ML array is fabricated on a PU spacer via multiple soft moulding processes (Extended Data Fig. 4). Figure 2o shows the g-ML surface, and incident light can be focused onto the Si PD regardless of external RI changes (Fig. 2p,q).

Assembled artificial vision system for panoramic imaging

As the ocular shape of the fiddler crab eye determines the equatorial spatial resolution and vertical FoV (FoV_V)¹⁰, ray density simulations were performed for three ocular structures (Fig. 3a,b) to optimize the ocular shape of artificial vision. Supplementary Note 2 provides the simulation details. In the prolate structure, which is similar to the fiddler crab eye, a high density of rays is found near the equator, but rays are not observed at a large FoV_V (Fig. 3b, top). In contrast, in the oblate structure, rays can be found at a large FoV_V (such as 70° or -70°), but the density of the equatorial ray decreases drastically, compared with that of the prolate structure (Fig. 3b, bottom). In the spherical structure, a balance between these two can be obtained (Fig. 3b, middle). Thus, the spherical structure was chosen for the 3D substrate structure to consider both viewing angle coverage and equatorial spatial resolution. The optical simulations for various ocular shapes display the trade-off relation between the FoV_V and horizontal ray density (density within FoV_V range of approximately -30° to 30°) (Fig. 3c). In nature, some compound eyes have evolved

to have various ellipsoidal shapes (that is, prolate and oblate shapes) or spheres (Supplementary Table 3). The simulation result indicates that the diverse shapes of the eyes can offer various combinations of FoV_V and horizontal ray density. Hence, the different geometries of an artificial vision system can be designed and engineered according to the purpose of the application.

Figure 3d shows the artificial ommatidia integrated on a 3D spherical structure for panoramic vision. As the fiddler crab eye covers almost the entire visual space, the integrated device has pixels distributed over almost the entire 3D surface^{27,28}. A 3D structure with wedge grooves was fabricated using a 3D printer. The image sensor and microlens arrays were placed inside grooves for deterministic assembly in 3D space. The spacing and locations of grooves were designed by considering optical screening between adjacent pixels. Specifically, two adjacent grooves have a central angle difference of 20° from the top view (Fig. 3e, left) and horizontal visual field (FoV_H) covers 300° except the blank region for connection of the readout pad. From the side view (Fig. 3e, right), the vertical inter-ommatidial angle ($\Delta\phi_V$) was set to 10.55° , to avoid overlap between the visual fields of neighbouring pixels, considering the acceptance angle of g-ML ($\Delta\theta = 5.70^\circ$) (Extended Data Fig. 5a,b). The vertical visual field (FoV_V) covers 160° . Supplementary Note 3 provides details about the acceptance angle.

Four comb-shaped image sensor arrays integrated with g-MLs (two for the top hemisphere and two for the bottom hemisphere) were assembled on the 3D structure. Each image sensor array has eight comb-like subunits, and each subunit consists of eight pixels. Figure 3f shows the image sensor arrays for one hemisphere (two arrays are connected, containing 16 subunits and 128 pixels). Figure 3g provides an exploded view of the imaging device. The photodetector layers are shown at the bottom, and g-MLs and a PU spacer are shown on the top. The photodetector is composed of ultrathin silicon (thickness, $1.2\ \mu\text{m}$), metal traces (Cr/Au) and polyimide (PI) encapsulations. The g-ML array on the PU spacer is aligned with the photodetector array. Because the layers composing the g-ML have larger moduli than the base PU layer, the strain during assembly on the curved structure is negligible (Extended Data Fig. 5c–e). The proposed comb-shaped image sensor array design provides a high degree of freedom that can mimic even the outlandish eye geometries found in nature (Supplementary Table 3).

Figure 3h presents detailed images of the photodetector. The photodiode was designed as a lateral PIN-type diode^{29,30} with an interdigitated pattern. The width and length of the blocking diode are much smaller than those of the photodiode to limit the backward current. The ultrathin photodetector array maintained stable performance during its assembly on the 3D structure owing to its flexibility^{31,32}. The photoresponse of the photodiode is linear, exhibiting a sufficient difference between the on and off currents and is stable under mechanical bending deformations with various curvatures and independent of the surrounding materials (that is, air and water) (Supplementary Fig. 3). In principle, our system is based on the compound eye, and thus, it is difficult to have a higher spatial resolution than an imaging system imitating single-chambered eyes. However, the comb-shaped array can implement an artificial vision device with better spatial resolution through dense optical units, whose dimension is similar to the fiddler crab eye (Supplementary Figs. 4 and 5). Supplementary Note 4 discusses the potential of the high-density artificial vision system in more detail.

Amphibious and panoramic imaging of the artificial system

In biological systems, the compound eyes of fiddler crabs have a typical inter-ommatidial angle of $\sim 1^\circ$, although the angle varies with respect to the position in the compound eye²⁰. To mimic such a spatial resolution, a scanning method, which involves rotating the imaging device to have a desired inter-ommatidial angle, is exploited, and the scanning process was conducted to set the inter-ommatidial

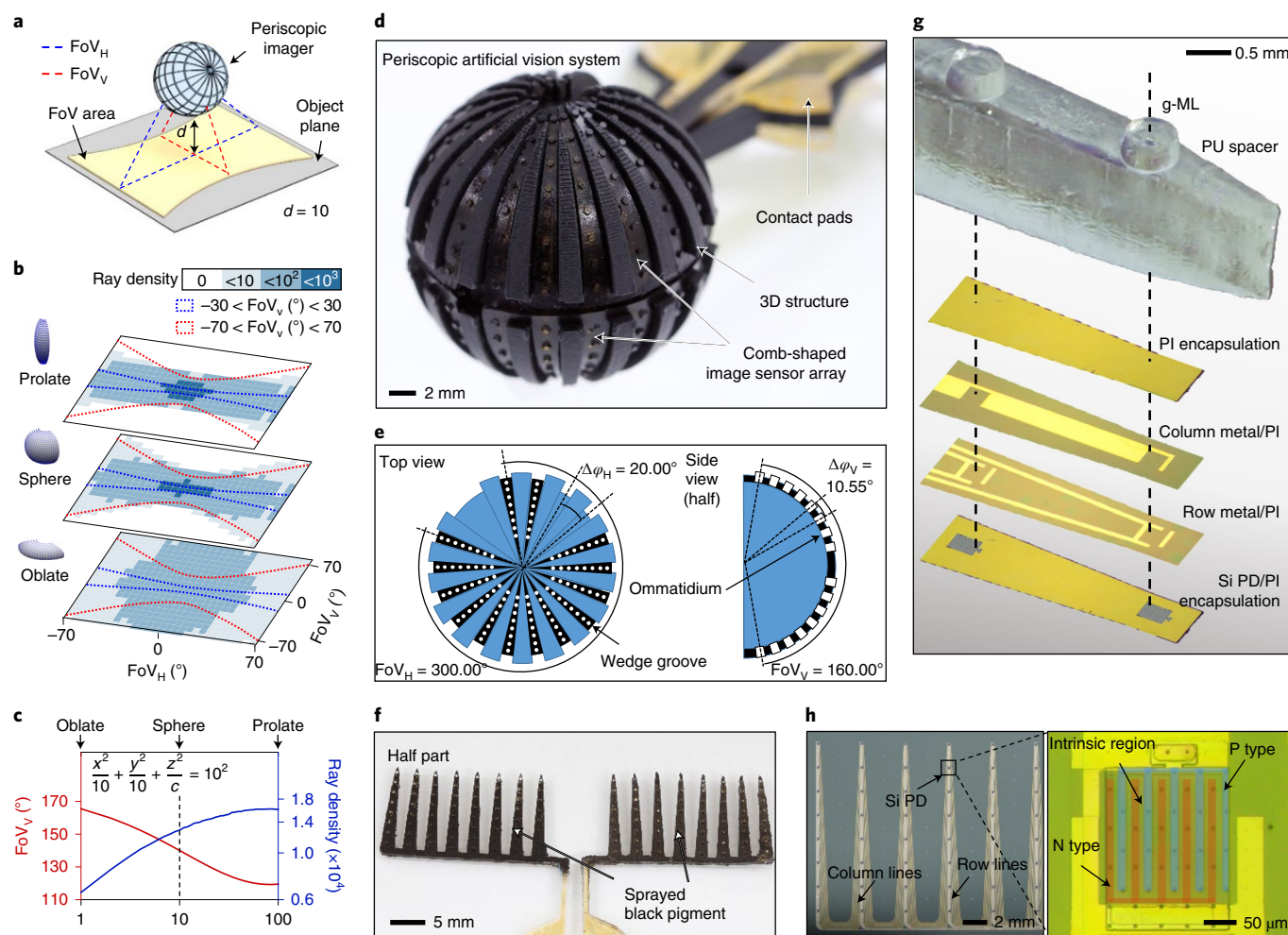


Fig. 3 | Integrated device on a 3D structure for panoramic imaging. **a**, Mapping of the incident rays on a 2D image plane. **b**, Simulation of the ray density distribution for various ocular structures. **c**, Simulations of FoV_V and horizontal ray density (in FoV_V range of approximately -30° to 30°) as a function of parameter c in the ellipsoidal equation. The oblate, spherical and prolate shapes in **b** correspond to c values of 1, 10 and 100, respectively. **d**, Photograph of artificial vision. Photodetectors and microlenses are integrated on the spherical 3D structure. The dots on the ellipsoid show the locations of the microlenses and photodetectors. **e**, Pixel distribution on the 3D structure from the top (left) and side (right) view. **f**, Comb-shaped image sensor array, which covers one hemisphere of the 3D structure. **g**, Exploded view of the comb-shaped image sensor array, which includes the polymeric microlens part (top) and photodetector part (bottom). **h**, Photograph of a photodetector array (left), and a magnified view of the photodiode with a lateral PIN structure (right).

angle of 1° . Supplementary Note 5 provides more details of the scanning method⁵. Various imaging conditions were explored through simulations to find an optimum condition (Extended Data Fig. 6). Figure 4a presents a simulation (left) and the corresponding experiment (right) for imaging, as rendered on a spherical surface with the same size as the artificial vision system. The inset shows the original image (crab pattern). The experimentally obtained image is consistent with the simulated image. For the simulation, the ideal characteristic parameters of the artificial vision system were used. Parasitic scattering within the artificial vision design can cause a partial loss of resolution and edge definition⁵. Supplementary Note 6 describes details of the imaging simulation.

The artificial vision system features an extremely wide FoV without off-axis aberrations owing to the microscale lens and spherical apposition design. Figure 4b presents a quantitative analysis of the FoV, which was performed using laser illuminations at points with angles between -120° and 120° by 120° intervals in the horizontal direction and with angles between -90° and 90° by 30° intervals in the vertical direction. Due to the geometrical advantage of the artificial vision system, laser spots can be imaged over the entire visual

field, except at the posterior blind spot for the data readout connection. The visual-field simulation results show that a larger number of ommatidia contribute to the imaging when $\Delta\theta$ and $\Delta\phi$ are wider and narrower, respectively (Extended Data Fig. 7a–d). Additional simulations confirm that optimum angular values exist depending on the object distance (Extended Data Fig. 7e–g).

The imaging of five objects with different distances and directions (Fig. 4c) demonstrates the panoramic nature of artificial vision. Figure 4d shows an exploded view of the imaging results. The shapes, sizes and positions of the experimentally obtained images match well with the simulation results (Extended Data Fig. 8). These results show the uniform imaging capability with minimum optical aberrations and a wide FoV (that is, FoV_V of 160° and FoV_H of 300°). To obtain equivalent imaging results using a conventional optical system with planar image sensors is challenging because of high off-axis aberrations, particularly due to geometric distortion^{33,34}. Moreover, a modulation transfer function of the imaging device is simulated and measured using the USAF1951 target. The higher modulation transfer function (that is, sharpened image) requires smaller $\Delta\theta$ (Supplementary Figs. 6 and 7).

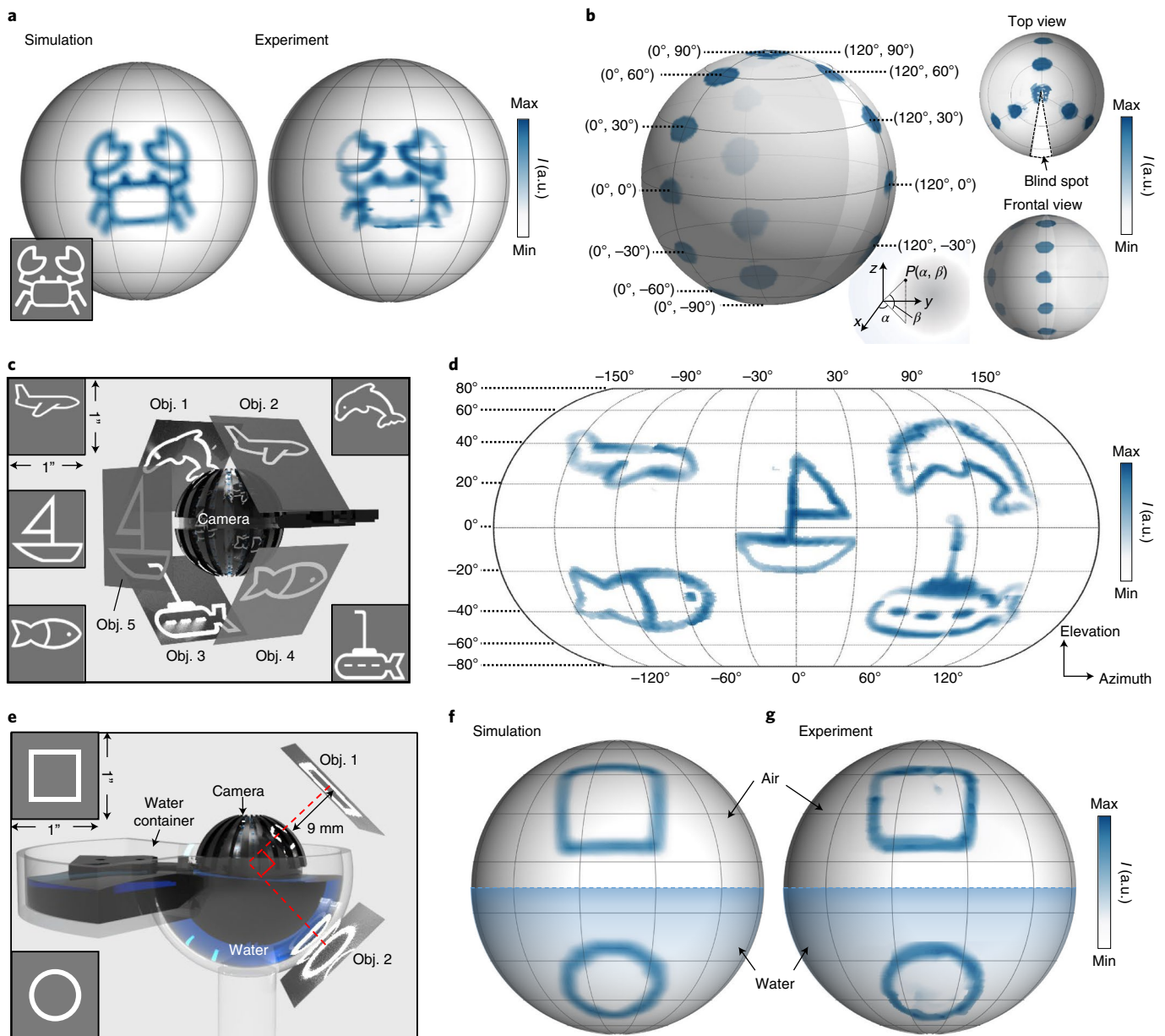


Fig. 4 | Amphibious and panoramic imaging demonstration. **a**, Crab pattern (original image is shown in the inset) obtained by optical simulation (left; simulation) and artificial vision (right; experiment). The width and height of the object are one inch each. **b**, Images obtained by artificial vision for three sequential illuminations of six collimated laser beams are merged into one image. Six laser beams were irradiated from six different incident angles between -90° and 90° with intervals of 30° . The right insets show the top and front view of the merged image. **c**, Experimental setup for the panoramic imaging demonstration. Five objects (dolphin, airplane, submarine, fish and ship labelled Obj. 1–5, respectively) located at different distances (airplane, dolphin and fish at a distance of 6 mm; submarine and ship at a distance of 8 mm) were projected onto the artificial vision system from different angles. **d**, Exploded view of the panoramic imaging result. **e**, Experimental setup for the amphibious imaging demonstration. Two objects (Obj. 1 and Obj. 2) located at a distance of 9 mm were projected onto the artificial vision system with an angular difference of 90° . A transparent water container was filled halfway to create the amphibious environment. **f**, Image obtained by optical simulation. **g**, Image obtained by artificial vision in an amphibious (air–water) environment.

Figure 4e provides a schematic of the experimental setup for the amphibious and panoramic imaging system. To emulate the living environment of a fiddler crab, the device was installed in a container filled halfway with water. A parylene C layer (thickness, $\sim 1 \mu\text{m}$) was deposited on the assembled device by chemical vapour deposition for encapsulation. Two objects were projected from different directions to mimic the amphibious visual space of the fiddler crab. The water container was composed of a clear tough resin and fabricated by a 3D printer. Shadow masks with circular and square line

art were placed on two planar light sources, located with an angular difference of 90° and at a distance of 9 mm.

Figure 4f shows the simulation results obtained with the ideal characteristic parameters of the artificial vision system in the air–water environment. The artificial vision system showed consistent imaging capabilities in this environment (Fig. 4g). The square images were obtained in air without the off-axis aberration, and the circular patterns were clearly imaged in water without optical aberrations and maintaining the wide FoV. Due to the unique design of

g-ML, external medium changes do not degrade the imaging quality or FoV. However, conventional h-ML loses the focusing feature and is unable to focus the incoming light, when the environment changes between air and water (Supplementary Fig. 8). According to these demonstrations, all-weather imaging can be achieved with the artificial vision system. A comparison of the artificial vision system with conventional panoramic imaging systems (Supplementary Note 7 and Supplementary Fig. 9) further highlights its excellence.

Conclusions

We have reported amphibious and panoramic artificial vision inspired by the structural and functional features of the fiddler crab eye. Based on an analysis of the fiddler crab lens, we developed a flat microlens with a graded RI structure for amphibious focusing. To emulate the panoramic vision of the fiddler crab, we integrated graded microlens arrays with flexible Si PD arrays on a 3D spherical structure. The amphibious and panoramic imaging capabilities of artificial vision were verified via in-air and in-water demonstrations. Our system could be of use in the development of unconventional applications such as panoramic motion detection and obstacle avoidance in continuously changing environments. Valuable extensions of the approach include the consideration of biologically inspired light adaptation³⁵ schemes and further engineering to achieve higher resolution and superior image processing techniques.

Methods

Preparation of eye specimens and their characterization. An adult male *Uca arcuata* was anaesthetised by cooling it for 5 min in a deep freezer, and the eye stalks were cut as close as possible to the eyes by using a surgical knife. The eyes were fixed in Karnovsky's fixative solution for 24 h at room temperature. Post-fixation occurred in 1% osmium tetroxide (OsO_4) solution (0.1 M cacodylate buffer) for 2 h, followed by three 15 min washings in distilled water. The eyes were dehydrated through sequential washing in 70%, 80%, 90%, 95% and 100% (twice) ethanol for 15 min each. Then, for TEM imaging, the specimens were gradually infiltrated with a resin (Spurr's resin) through infiltration by (1) pure propylene oxide for 1 h, (2) 25%/75% resin/propylene oxide for 2 h, (3) 50%/50% resin/propylene oxide (overnight), (4) 75%/25% resin/propylene oxide for 2 h and (5) pure resin for at least 6 h. Polymerization was performed at 60 °C for 24 h. The specimens were imaged and characterized using an optical camera, optical microscope and electron microscope. A field-emission scanning electron microscope (Sigma, Carl Zeiss), which is installed at the National Instrumentation Center for Environmental Management at Seoul National University, was used to image the structure of the crab's eye. A cryo-TEM instrument (Tecnai F20 G², FEI), which is installed at the Korea Institute of Science and Technology, was employed to image the ultrathin section of the fixed eye. This experiment was approved by the Institutional Animal Care and Use Committee (SNU-210526-4) of Seoul National University.

Visual map reconstruction of the fiddler crab eye. A sample of a fiddler crab eye with a stalk was prepared for SEM imaging. The sample was mounted on a rotating SEM specimen holder (Supplementary Fig. 10a). The SEM images of the fiddler crab eye were taken with angular intervals of 45°. Using a custom-made code, the features of the facet lens were extracted from each image and deployed in two-dimensional (2D) space. The image tiles were horizontally aligned to create a panoramic image. In addition, the SEM images of the fiddler crab eye were vertically stitched together. Finally, a visual map of the fiddler crab eye was reconstructed in 2D space by merging the horizontally and vertically stitched images into a single image (Supplementary Fig. 10b).

Optical simulation for design and analysis of MLs. Monte Carlo-based 3D ray-tracing software (OpticStudio 16.0, Radiant ZEMAX) was exploited to design the g-ML and h-ML and analyse their optical characteristics. A rectangular detector ($80 \times 480 \mu\text{m}^2$) with 100×600 pixels was used to analyse the focusing performance of h-ML and g-ML. Optical simulations with various conditions were conducted to compare the images formed by h-ML and g-ML in air and water. For the simulation, 4×10^9 rays of monochromatic light (that is, $\lambda = 550 \text{ nm}$) were launched from the letter 'E' in non-sequential ray tracing (Supplementary Fig. 11). Further, h-ML and each layer of g-ML (base lens and the first, second and third lens layers) were computationally investigated in terms of the focal length by varying the RoCs of the four lens surfaces in air and water (Supplementary Fig. 12). In addition, the Seidel spherical aberration was analysed for various RoCs of the four lens surfaces (Supplementary Fig. 13). Based on these simulation results, the g-ML design to reduce spherical aberration was determined by increasing the RoC with a low sag height.

Fabrication of g-ML array for lens characterization. Three layers of optical adhesives (Norland optical adhesive (NOA) 133, 13685 and 138 for diameters of 17 and $80 \mu\text{m}$ and 1348, 1379 and 139 for diameter of $400 \mu\text{m}$; Norland Products) and a base microlens (h-ML) array made of a clear elastomer (SYLGARD 184, Dow Corning; mixing ratio of 1:10 between the curing agent and prepolymer) were used to fabricate the g-ML array (Supplementary Table 2 provides the design specifications), which was fabricated by using multiple spin-coating processes. The theoretical analysis results showed that the fabricated g-MLs were robust against RoC variations that can occur in multiple spin-coating processes (Supplementary Fig. 13). Supplementary Fig. 14 and Supplementary Table 4 show the corresponding schematic and processing conditions, respectively. Master quartz moulds were fabricated via HF etching of quartz using a silicon mask with hole patterns. After removing the silicon mask with KOH, HF etching was repeated to obtain a large curvature³⁶. The elastomer was poured onto and cured on the mould at 70 °C for 6 h to fabricate the base lens (Supplementary Fig. 15). To enhance the adhesion between optical adhesives (that is, NOAs) and the elastomer base lens, the elastomer surface was treated by O_2 plasma generated in the reactive ion etcher (40 s.c.c.m. , 100 W, 100 mtorr). Different materials and rotation speeds were used to fabricate the microlens arrays with various diameters. For example, NOA was spin coated onto the elastomer base lens and cured by ultraviolet (UV) irradiation under a N_2 environment (365 nm; dose, 6 J cm^{-2} ; N_2 flow, 2 l min^{-1}). These spin-coating and curing processes were repeated three times to fabricate the g-ML array.

Fabrication of g-ML array for the imaging device. Three layers of optical adhesives (NOA 1348, 1369 and 139; Norland Products) and a base elastomer layer (Clear Flex 50; Smooth-On) were used to fabricate the g-ML array for the integrated imaging device. The g-ML array was produced via multiple soft moulding processes (Extended Data Fig. 4). Soft moulds were made of silicone (Ecoflex, Smooth-On). The soft moulds for the middle lenses (first and second lenses) were designed to have composite shapes of cavities (cylinders with hemispherical tops), and the soft mould for the flat top layer (third lens) was designed to have a hollow cylinder shape (Supplementary Table 5). The base lens and soft moulds were aligned and brought into contact with each other to confine the NOA in the space between the base lens and soft mould. The confined NOA was cured by UV irradiation (365 nm; dose, 6 J cm^{-2}). Residual NOA was removed using tweezers. The UV irradiation is sufficient to bond the NOAs and PU because they are based on the same material, namely, urethane. The alignment and UV irradiation process were repeated to complete the fabrication of the g-ML array. An SP layer was deposited onto the entire surface by spray coating. Then, the SP on the lens area was peeled off by bringing it into contact with a glass stamp coated with an organic solvent.

Fabrication of comb-shaped image sensor array. First, a silicon-on-insulator (top silicon, $1.25 \mu\text{m}$, SOITEC) wafer was doped using spin on dopants to define the n-type and p-type regions. After the doping process, the silicon nanomembrane was transferred onto a PI layer (thickness, $\sim 2 \mu\text{m}$) coated on a SiO_2 wafer. The active regions for the photodiodes were isolated using photolithography and dry etching. A PI layer (thickness, $\sim 1 \mu\text{m}$) was spin coated for the intermediate dielectric layer. Vertical interconnect access patterns were formed, and metallization (first metal interconnect, Cr/Au layers, $10/100 \text{ nm}$) was performed. Additional depositions of the PI and metal layer and patterning of the metal layer (second metal interconnect) were conducted by using the same process. Supplementary Fig. 16 shows the layouts for the metal interconnections. As a top encapsulation layer, a PI layer (thickness, $\sim 1 \mu\text{m}$) was deposited by spin coating and then the entire device was etched into a comb-shaped pattern. The fabricated comb-shaped image sensor array was detached from the SiO_2 wafer with a water-soluble tape (3M) and transfer printed onto an elastomer layer (Ecoflex). The top PI layer of the comb-shaped photodiode array and bottom surface of the base polymer layer (Clear Flex 50) were treated by O_2 plasma. Then, the comb-shaped photodiode array and base polymer layer were bonded.

Mechanical analysis of g-ML for the integrated device. Commercial software (Abaqus, standard 6.13) was employed to understand how much strain was applied to the panoramic image sensor, especially to the microlens arrays, under bending. The cross section of the multilayer device was modelled using a 2D deformable shell with a four-node plane stress element (CPS4). Each layer was partitioned accordingly, and it was assumed that there was no delamination at the interface. For the microlens array ($h_{\text{lens}} = 270 \mu\text{m}$) and PU spacer ($h_{\text{PU}} = 1.2 \text{ mm}$), incompressible neo-Hookean hyperelastic material was assigned with material properties of $E_{\text{NOA1348}} = 54.9 \text{ MPa}$, $E_{\text{NOA1369}} = 12.8 \text{ MPa}$, $E_{\text{NOA139}} = 44.9 \text{ MPa}$ and $E_{\text{PU}} = 1.0 \text{ MPa}$. The photodiode layer composed of multiple thin layers of metals and PI was modelled as a simplified single layer because (1) it has a negligible effect to the strain distribution on the microlens arrays under bending and (2) it was not the area of interest. Incompressible neo-Hookean elastic material was assigned to the photodiode layer with an effective modulus of

$$E_{\text{Eff}} = E_{\text{PI}} \left(\frac{h_{\text{PI}}}{h_{\text{PI}} + h_{\text{Au}} + h_{\text{Si}}} \right) + E_{\text{Au}} \left(\frac{h_{\text{Au}}}{h_{\text{PI}} + h_{\text{Au}} + h_{\text{Si}}} \right) + E_{\text{Si}} \left(\frac{h_{\text{Si}}}{h_{\text{PI}} + h_{\text{Au}} + h_{\text{Si}}} \right),$$

where $E_{PI} = 2.5$ GPa, $E_{Au} = 79.0$ GPa, $E_{Si} = 179.0$ GPa, $h_{PI} = 4.50$ μm , $h_{Au} = 0.20$ μm and $h_{Si} = 1.25$ μm .

Amphibious and panoramic imaging demonstration. A customized measurement setup was used to demonstrate the amphibious and panoramic imaging capabilities of artificial vision. For panoramic imaging, omnidirectional objects were implemented by four flat diffusive light sources (MB-TBL1X1-W-24CV, Vision Light Tech). In addition, multilaser spot imaging experiments were conducted (Supplementary Fig. 17). Amphibious imaging was performed by immersing the device halfway in water in a water container. The scanning method⁴ was exploited to improve the imaging resolution. The artificial vision system was rotated from -10.00° to 10.00° with increments of 1.00° about the z axis and from -5.30° to 5.30° with increments of 0.53° about the x and y axes, respectively. Three motorized stages constituted the scanning setup (Supplementary Fig. 18). A data acquisition board supported real-time data acquisition and transferred the data to a computer (Supplementary Fig. 19). Supplementary Notes 1–7 provide more details.

Data availability

The data that support the plots within this paper and other findings of this study are available from the corresponding authors upon reasonable request.

Code availability

The source codes for MATLAB are available from the corresponding authors upon request.

Received: 31 August 2021; Accepted: 27 May 2022;

Published online: 11 July 2022

References

- Ko, H. C. et al. A hemispherical electronic eye camera based on compressible silicon optoelectronics. *Nature* **454**, 748–753 (2008).
- Choi, C. et al. Human eye-inspired soft optoelectronic device using high-density MoS_2 -graphene curved image sensor array. *Nat. Commun.* **8**, 1664 (2017).
- Gu, L. et al. A biomimetic eye with a hemispherical perovskite nanowire array retina. *Nature* **581**, 278–282 (2020).
- Rao, Z. et al. Curvy, shape-adaptive imagers based on printed optoelectronic pixels with a kirigami design. *Nat. Electron.* **4**, 513–521 (2021).
- Song, Y. M. et al. Digital cameras with designs inspired by the arthropod eye. *Nature* **497**, 95–99 (2013).
- Zhang, K. et al. Origami silicon optoelectronics for hemispherical electronic eye systems. *Nat. Commun.* **8**, 1782 (2017).
- Kim, M. S. et al. An aquatic-vision-inspired camera based on a monocentric lens and a silicon nanorod photodiode array. *Nat. Electron.* **3**, 546–553 (2020).
- How, M. J. et al. Target detection is enhanced by polarization vision in a fiddler crab. *Cur. Biol.* **25**, 3069–3073 (2015).
- Smolka, J. & Hemmi, J. M. Topography of vision and behavior. *J. Exp. Biol.* **212**, 3522–3532 (2009).
- Alkaladi, A. & Zeil, J. Functional anatomy of the fiddler crab compound eye (*Uca vomeris*: Ocypodidae, Brachyura, Decapoda). *J. Comp. Neurol.* **522**, 1264–1283 (2014).
- Bryceson, K. P. Focusing of light by corneal lenses in a reflecting superposition eye. *J. Exp. Biol.* **90**, 347–350 (1981).
- Nilsson, D.-E. Three unexpected cases of refracting superposition eyes in crustaceans. *J. Comp. Physiol. A* **167**, 71–78 (1990).
- Horváth, G. Geometric optical optimization of the corneal lens of *Notonecta glauca*. *J. Theor. Biol.* **139**, 389–404 (1989).
- Jang, H. J. et al. Double-sided anti-reflection nanostructures on optical convex lenses for imaging applications. *Coatings* **9**, 404 (2019).
- Zeil, J., Hemmi, J. M. & Backwell, P. R. Y. Fiddler crabs. *Curr. Biol.* **16**, R40–R41 (2006).
- Castro, P., Davie, P., Guinot, D., Schram, F. R. & von Vaupel Klein, J. C. *The Crustacea*. in *Treatise on Zoology—Anatomy, Taxonomy, Biology* Vol. 9 (Brill, 2015).
- Ng, P. K. L., Schubart, C. D. & Lukhaup, C. New species of ‘vampire crabs’ (*Geosesarma* De Man, 1892) from central Java, Indonesia, and the identity of *Sesarma* (*Geosesarma*) *nodulifera* De Man, 1892 (Crustacea, Brachyura, Thoracotremata, Sesarmidae). *Raffles Bull. Zool.* **63**, 3–13 (2015).
- Green, P. T. Field observations of moulting and moult increment in the red land crab, *Gecarcoidea natalis* (Brachyura, Gecarcinidae), on Christmas Island (Indian Ocean). *Crustaceana* **77**, 125–128 (2004).
- Nilsson, D. E. A new type of imaging optics in compound eyes. *Nature* **332**, 76–78 (1988).
- Arikawa, K., Kawamata, K., Suzuki, T. & Eguchi, E. Daily changes of structure, function and rhodopsin content in the compound eye of the crab *Hemigrapsus sanguineus*. *J. Comp. Physiol. A* **161**, 161–174 (1987).
- McLay, C. L. Brachyura and crab-like Anomura of New Zealand. *Leigh Lab. Bull.* **22**, 463 (1988).
- Eguchi, E., Dezawa, M. & Meyer-Rochow, V. B. Compound eye fine structure in *Paralomis multispina* Benedict, an anomuran half-crab from 1200 m depth (Crustacea; Decapoda; Anomura). *Biol. Bull.* **192**, 300–308 (1997).
- Luque, J. et al. Evolution of crab eye structures and the utility of ommatidia morphology in resolving phylogeny. Preprint at *bioRxiv* <https://doi.org/10.1101/786087> (2019).
- Cai, J., Townsend, J. P., Dodson, T. C., Heiney, P. A. & Sweeney, A. M. Eye patches: protein assembly of index-gradient squid lenses. *Science* **357**, 564–569 (2017).
- Alagboso, F. et al. Ultrastructure and mineral composition of the cornea cuticle in the compound eyes of a supralittoral and a marine isopod. *J. Struct. Biol.* **187**, 158–173 (2014).
- Kim, K., Jang, K.-W., Ryu, J.-K. & Jeong, K.-H. Biologically inspired ultrathin arrayed camera for high-contrast and high-resolution imaging. *Light. Sci. Appl.* **9**, 28 (2020).
- Lee, W. et al. Two-dimensional materials in functional three-dimensional architectures with applications in photodetection and imaging. *Nat. Commun.* **9**, 1417 (2018).
- Sim, K. et al. Three-dimensional curvy electronics created using conformal additive stamp printing. *Nat. Electron.* **2**, 471–479 (2019).
- Lee, W. et al. High-resolution spin-on-patterning of perovskite thin films for a multiplexed image sensor array. *Adv. Mater.* **29**, 1702902 (2017).
- Sheng, X. et al. Silicon-based visible-blind ultraviolet detection and imaging using down-shifting luminophores. *Adv. Opt. Mater.* **2**, 314–319 (2014).
- Kim, J. et al. Stretchable silicon nanoribbon electronics for skin prosthesis. *Nat. Commun.* **5**, 5747 (2014).
- Song, E. et al. Flexible electronic/optoelectronic microsystems with scalable designs for chronic biointegration. *Proc. Natl Acad. Sci. USA* **116**, 15398–15406 (2019).
- Hughes, C., Glavin, M., Jones, E. & Denny, P. Review of geometric distortion compensation in fish-eye cameras. In *IET Signals and Systems Conference (ISSC 2008)* 162–167 (IEEE, 2008).
- Liang, W.-L., Pan, J.-G. & Su, G.-D. J. One-lens camera using a biologically based artificial compound eye with multiple focal lengths. *Optica* **6**, 326–334 (2019).
- Brodrick, E. A., Roberts, N. W., Sumner-Ronney, L., Schleputz, C. M. & How, M. J. Light adaptation mechanisms in the eye of the fiddler crab *Afruca tangeri*. *J. Comp. Neurol.* **529**, 616–634 (2021).
- Kim, H. M., Kim, M. S., Lee, G. J., Yoo, Y. J. & Song, Y. M. Large area fabrication of engineered microlens array with low sag height for light-field imaging. *Opt. Express* **27**, 4435–4444 (2019).

Acknowledgements

This research was supported by IBS-R006-A1. This research was also supported by the National Research Foundation (NRF) of Korea (2017M3D1A1039288 and 2021R1A6A3A01087961) and the GIST-MIT Research Collaboration grant funded by the GIST in 2022.

Author contributions

M.L., G.J.L., H.J.J., D.-H.K. and Y.M.S. designed the experiments, analysed the data and wrote the paper. M.L. and H.C. prepared the biological specimens. J.H.L. performed the electron microscopy experiments. M.L., H.C., E.J. and M.K. fabricated the photodiode array and performed the characterization of individual devices. M.L. and H.C. performed the assembly of devices. G.J.L., H.J.J., M.S.K., H.M.K. and J.-E.Y. performed the theoretical and experimental analysis of the optics. G.J.L., H.J.J., K.M.K. and F.D. conducted the imaging simulation and demonstration. H.J. and N.L. performed the theoretical analysis of the mechanics. All the authors discussed the results and commented on the manuscript.

Competing interests

The authors declare no competing interests.

Additional information

Extended data is available for this paper at <https://doi.org/10.1038/s41928-022-00789-9>.

Supplementary information The online version contains supplementary material available at <https://doi.org/10.1038/s41928-022-00789-9>.

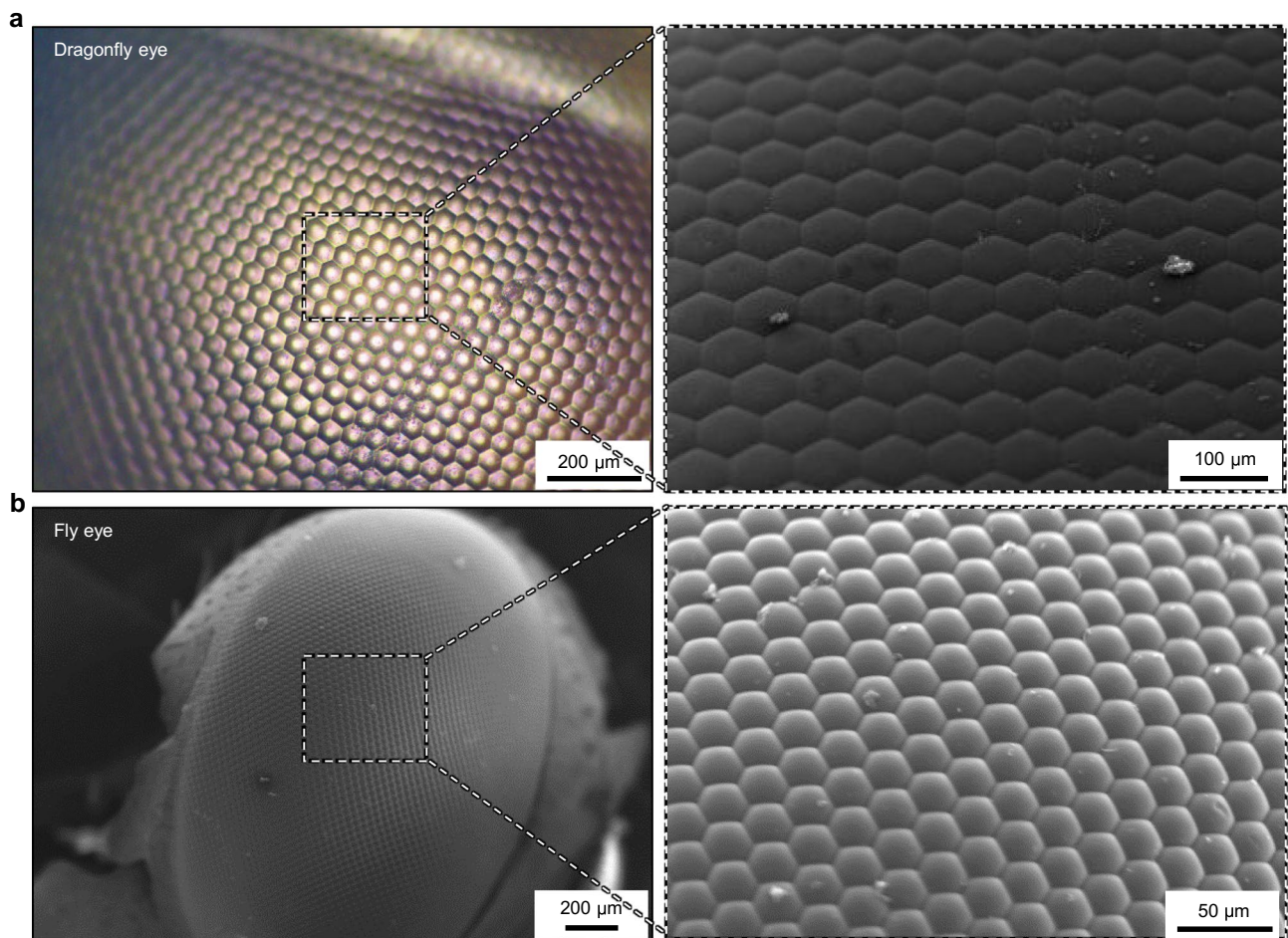
Correspondence and requests for materials should be addressed to Dae-Hyeong Kim or Young Min Song.

Peer review information *Nature Electronics* thanks Guo-Dung Su and the other, anonymous, reviewer(s) for their contribution to the peer review of this work.

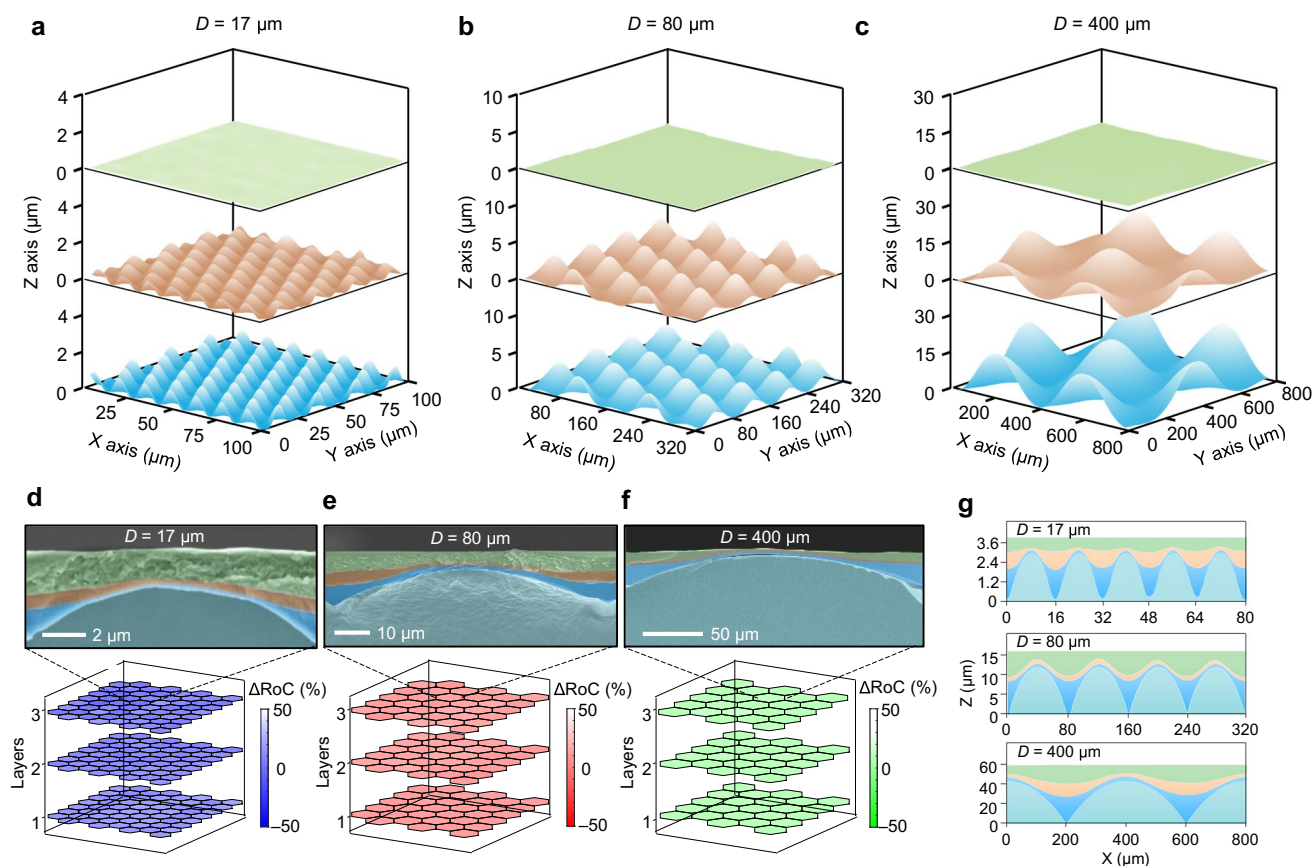
Reprints and permissions information is available at www.nature.com/reprints.

Publisher's note Springer Nature remains neutral with regard to jurisdictional claims in published maps and institutional affiliations.

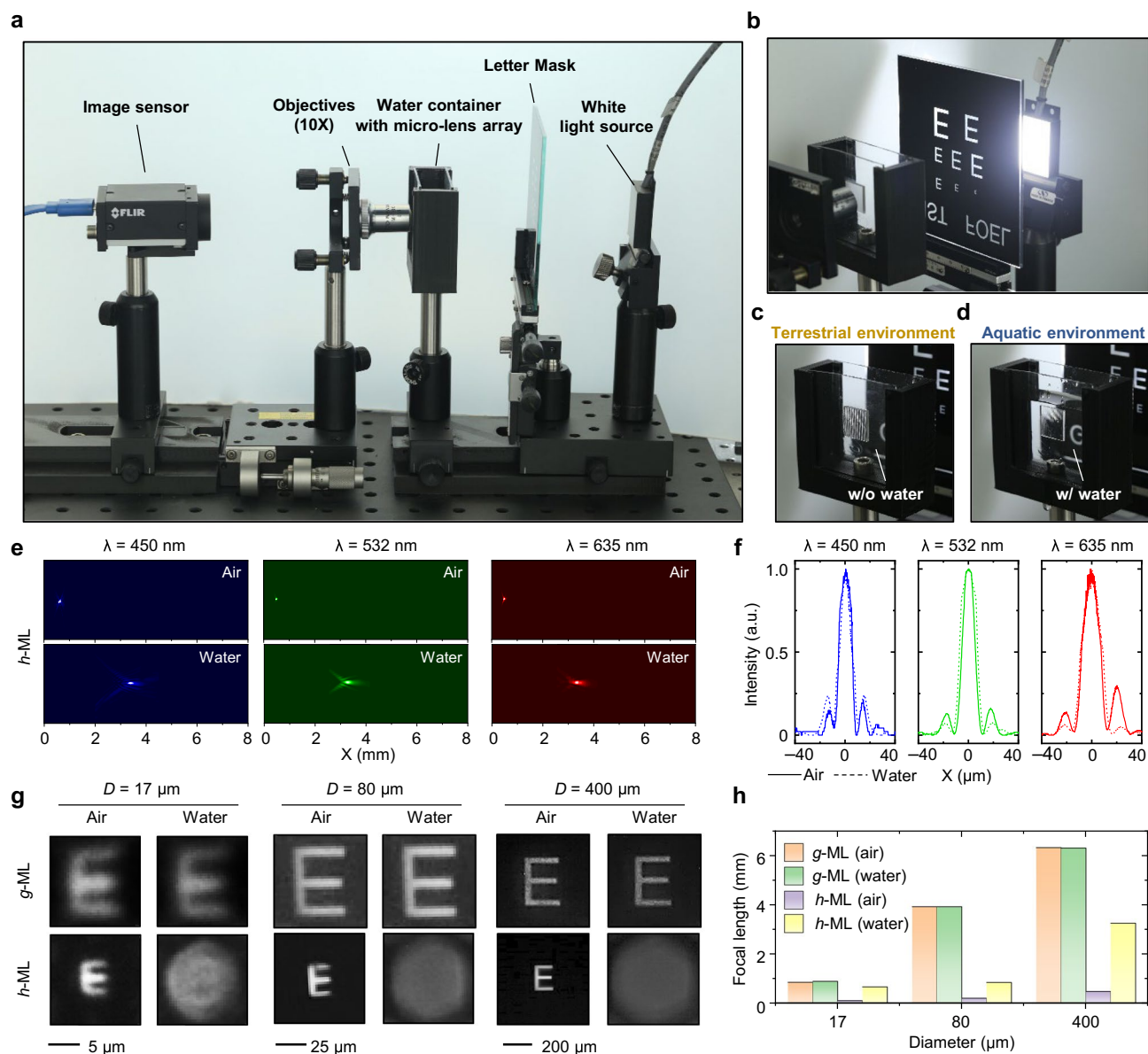
© The Author(s), under exclusive licence to Springer Nature Limited 2022



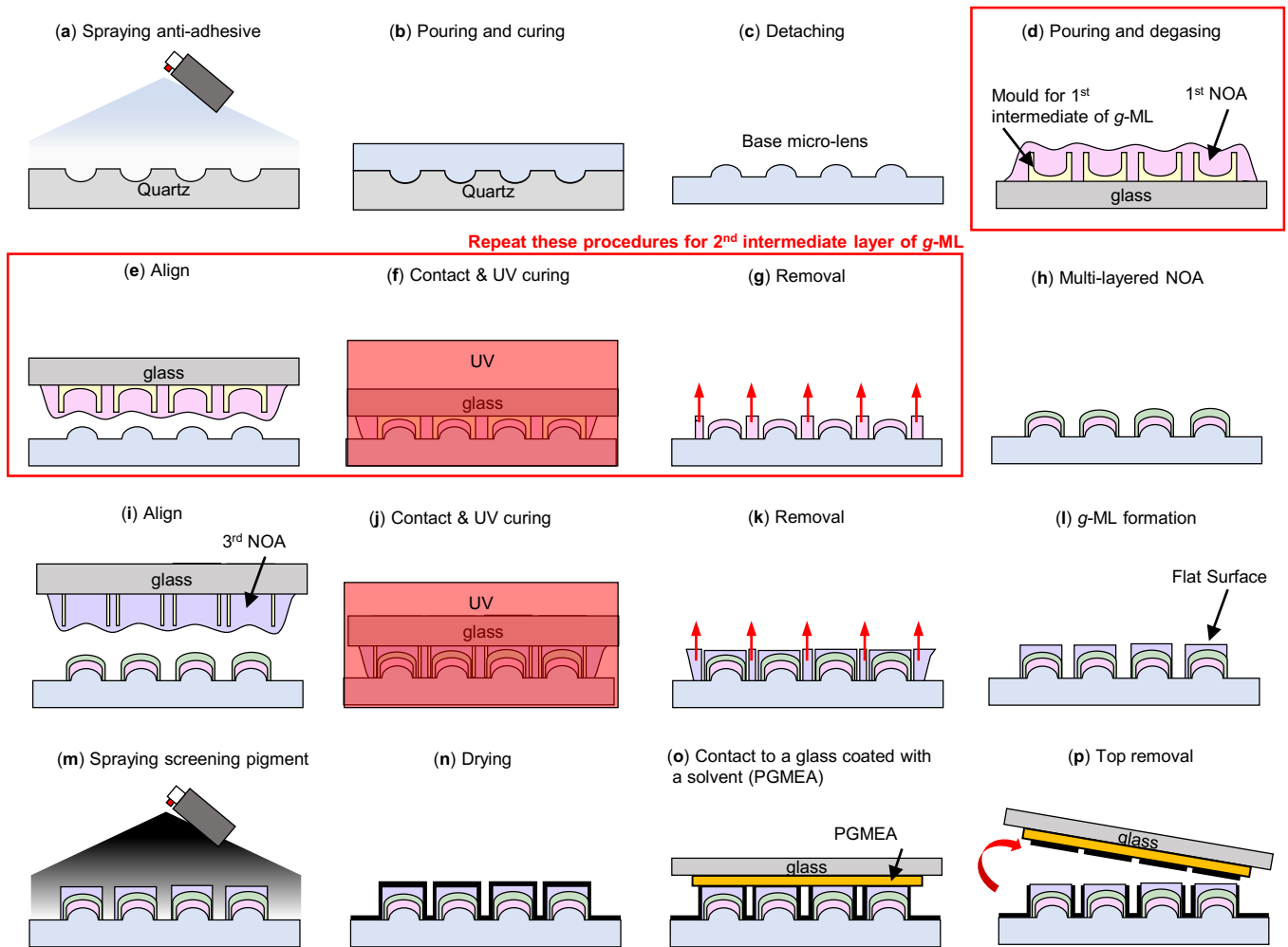
Extended Data Fig. 1 | Hemispherical (convex type) cornea facet lenses in the eyes of terrestrial arthropods. (a) Optical microscope images of a dragonfly eye (*Epophthalmia elegans*, left) and its SEM image (right). Its cornea facet lens has a convex-type hemispherical surface. (b) SEM images of a fly eye (*Calliphora vomitoria*, left) and its magnified view (right), which show the convex-type hemispherical surface of the cornea facet lens.



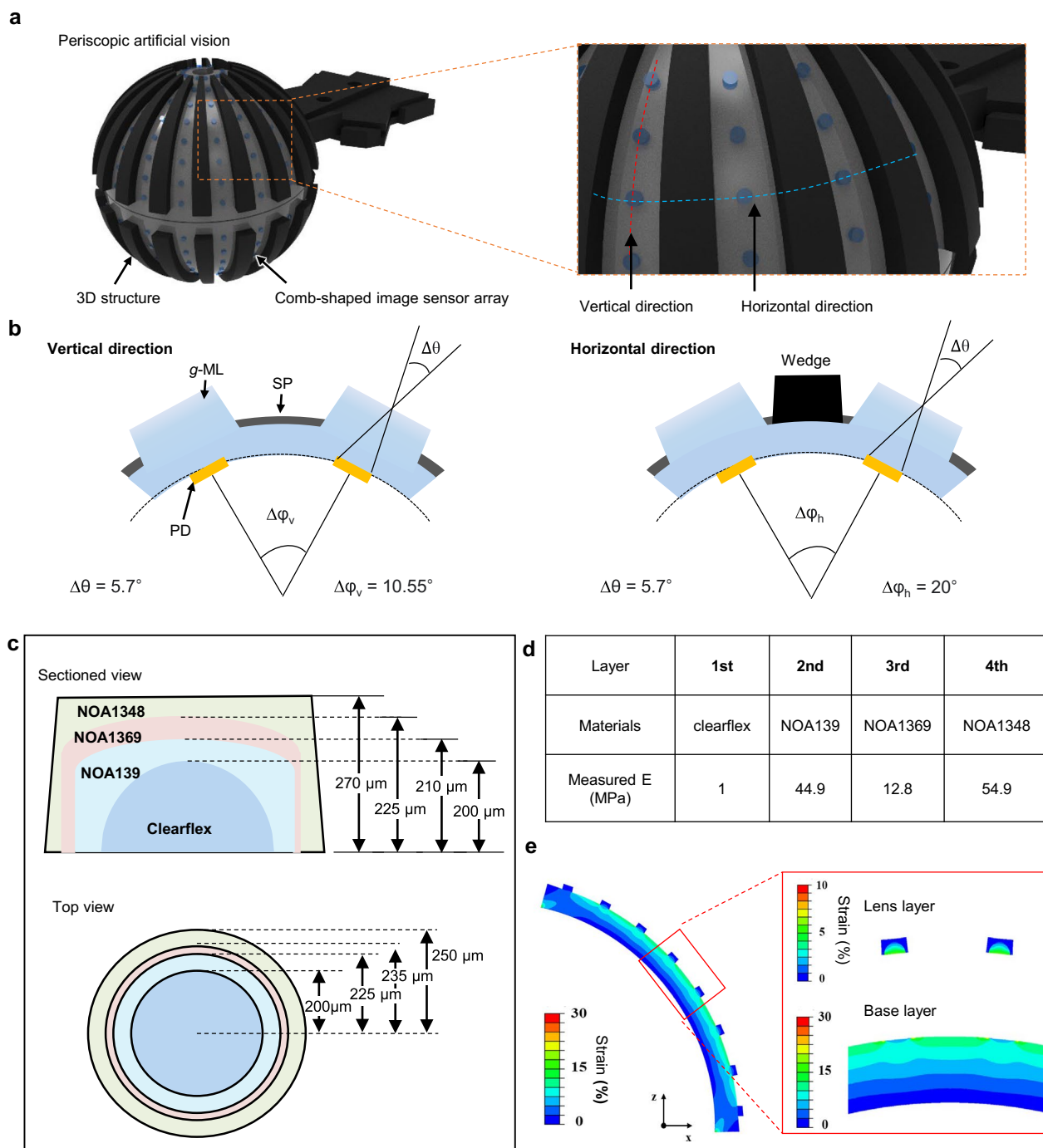
Extended Data Fig. 2 | Characterization of the fabricated *g*-ML arrays with various sizes. (a–c), Each layer of each *g*-ML array is scanned by confocal microscopy to reconstruct the 3D surface profile of each layer. The diameters (D) of the *g*-MLs are 17 μm (a), 80 μm (b), and 400 μm (c). (d–f) Colorized cross-sectional SEM images of the *g*-MLs (top) and deviations of the RoCs from the average RoCs in the *g*-ML layers (bottom) for three different micro-lens diameters, that is, 17 μm (d), 80 μm (e), and 400 μm (f). (g) 2D cross-sectional profiles of *g*-MLs with three different diameters (17 μm , 80 μm , and 400 μm in the top, middle, and bottom frames, respectively).



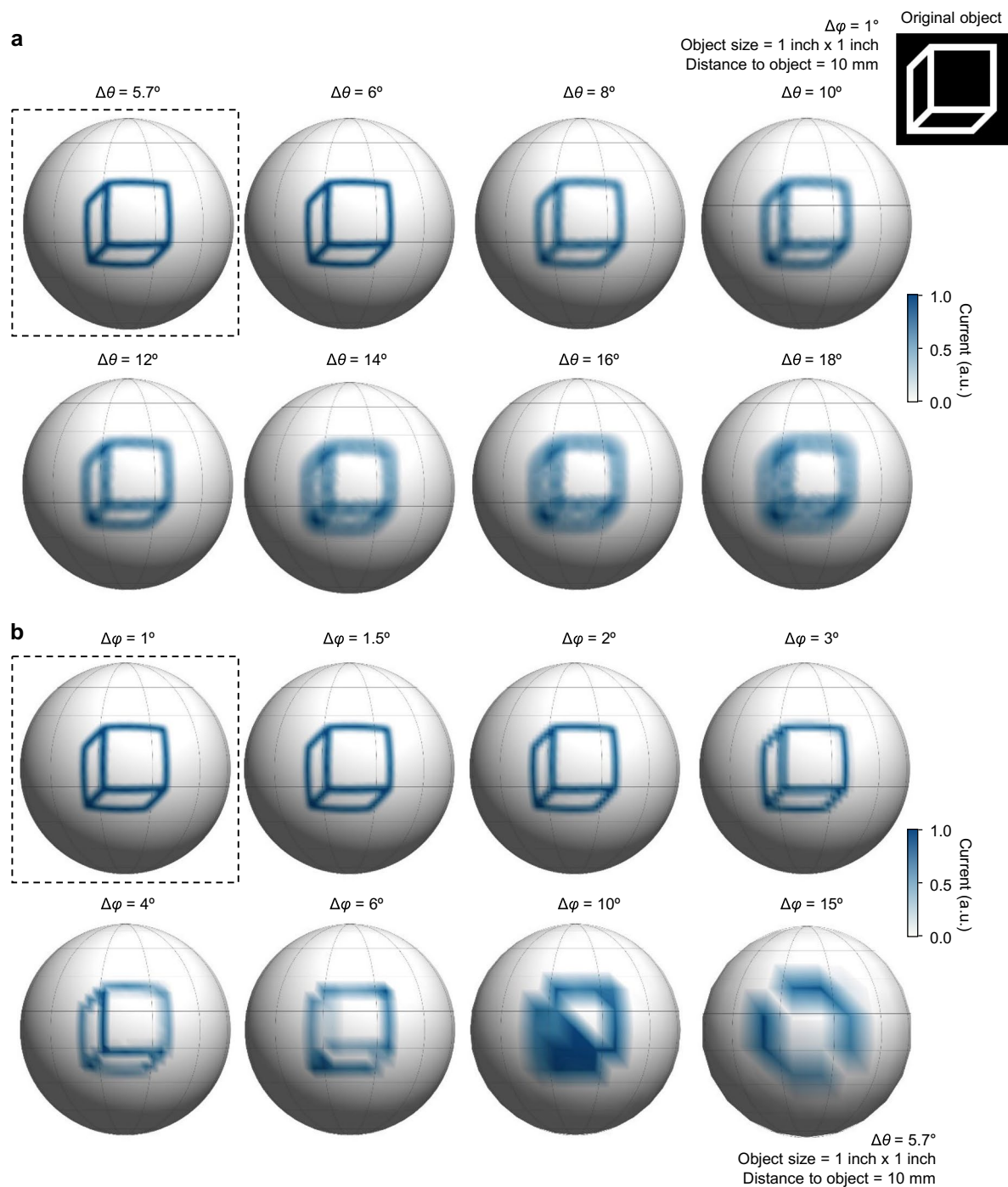
Extended Data Fig. 3 | Custom-made experimental setup for lens characterization in air and water, and measurement results. (a) Optical camera image of the custom-made experimental setup. The setup consists of a white light source or laser sources with wavelengths of 450, 532, and 635 nm; an objective lens (10 \times); and a CMOS image sensor. (b–d) Optical camera images showing the components, including the water container, for amphibious imaging. (e) Measured light intensity distribution of the *h*-ML (micro-lens size of 400 μm) for three wavelengths (left: 450 nm, centre: 532 nm, and right: 635 nm). (f) Cross-sectional light intensity profile of the *g*-ML with a micro-lens size of 400 μm at the focal length in air (solid line) and water (dotted line). These results show that the *g*-ML obtains identical profiles in both media at the same focal length. (g) Imaging results of a letter 'E' obtained by the *g*-ML (top) and *h*-ML (bottom) for various micro-lens sizes (that is 17, 80, and 400 μm) under white light. (h) Measured focal lengths of *g*-MLs and *h*-MLs with three sizes in air and water. For all sizes, the *g*-MLs show consistent focal lengths in air and water, whereas the *h*-MLs show large changes of their focal lengths between air and water.



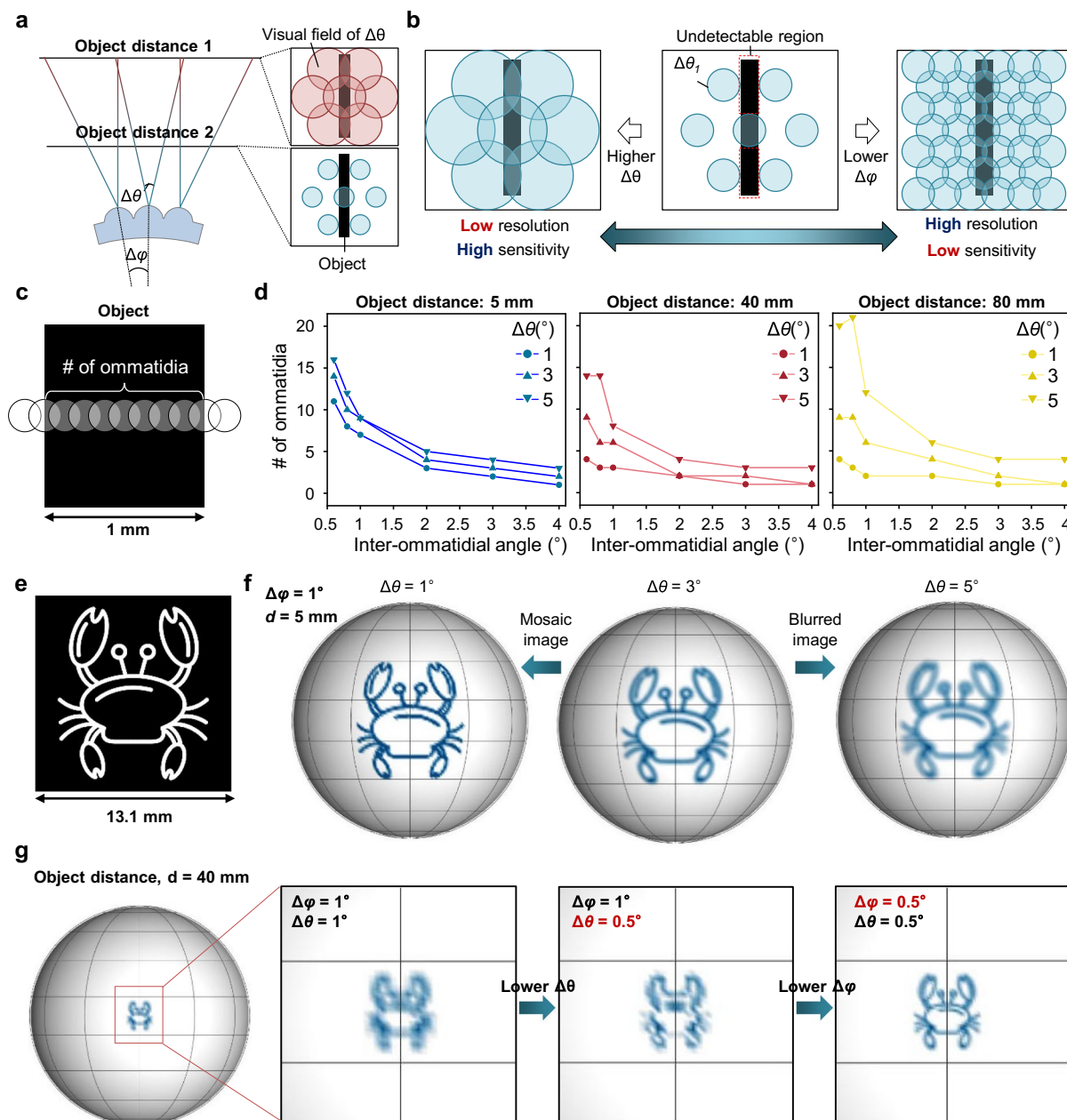
Extended Data Fig. 4 | Schematic illustrations of multiple soft moulding processes for the fabrication of the *g*-ML array. (a–c) Fabrication steps for a spacer layer and a base micro-lens array. (a) An anti-adhesive (Teflon AF™) is coated on a quartz mould. (b) The prepolymer (clear flex™ 50) for the spacer and base micro-lenses is poured onto the quartz mould and thermally cured for 20 h. (c) The spacer and base micro-lens layer is detached from the quartz mould. (d–g) Fabrication steps for intermediate lens layers of the *g*-ML. For intermediate *g*-ML layers, silicone (Ecoflex™) moulds of plano-concave shapes with different curvatures are prepared. These steps are repeated for two intermediate NOA layers. (d) NOA is poured onto the silicone mould, and air bubbles are removed. (e) The silicone mould and base micro-lenses are aligned using a microscope. (f) The silicone mould and base micro-lenses are brought into contact. NOA is cured by UV illumination. (g) The silicone mould is removed, and unnecessary NOA is removed using tweezers. (h) The multi-layered NOA structure is formed on the base micro-lens. (i–l) Fabrication steps for a flat *g*-ML surface. (i) The silicone mould for the flat surface lens is prepared. NOA for the flat surface lens is poured onto the silicone mould. The multi-layered lens and silicone mould are aligned using a microscope. (j) The silicone mould and the multi-layered lens are brought into contact. NOA is cured using UV radiation. (k) Unnecessary NOA is removed using tweezers. (l) A *g*-ML with a flat surface is fabricated. (m, n) The screening pigment (SP) is spray-printed onto the *g*-ML and dried. (o, p) For light transmission, the SP on the *g*-ML surface is removed by bringing it into contact with solvent-coated (propylene glycol methyl ether acetate) glass.



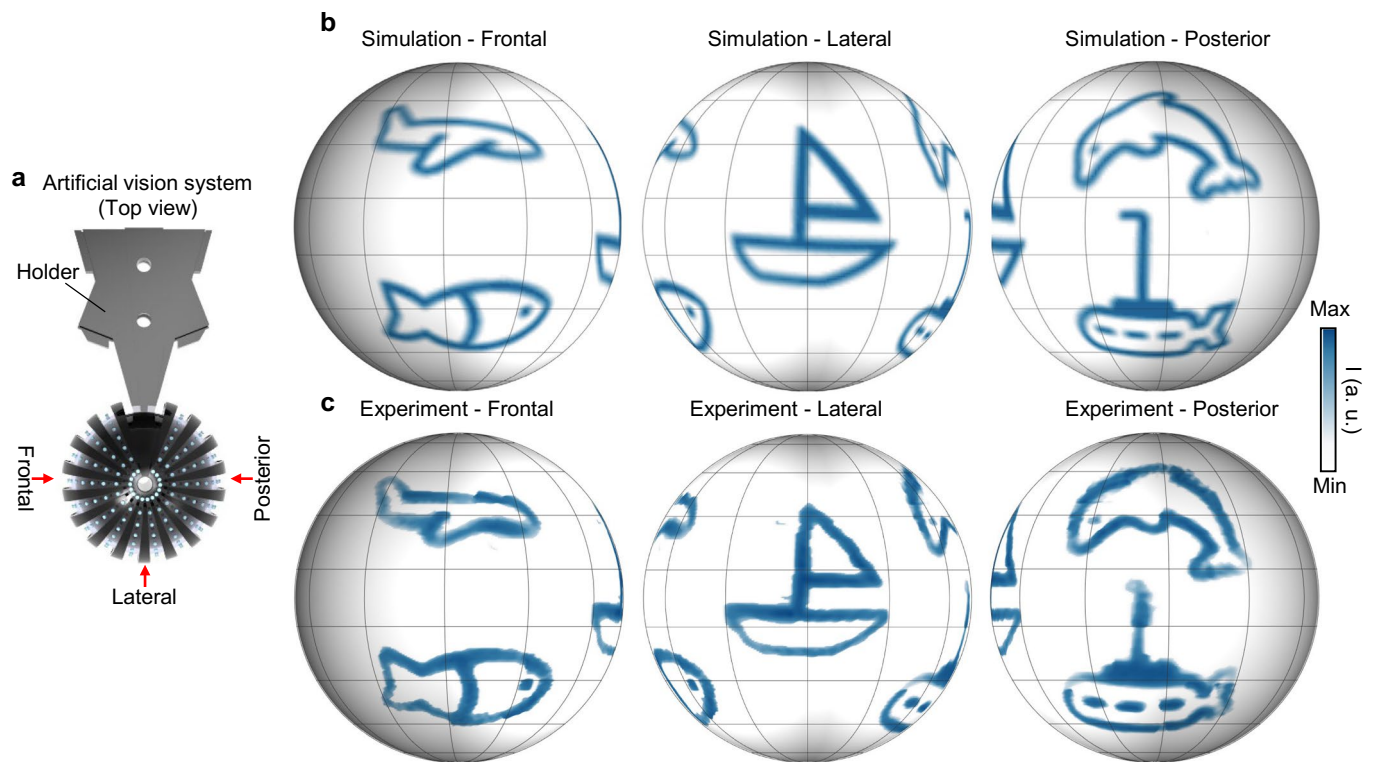
Extended Data Fig. 5 | Design of the panoramic artificial vision using the spherical 3D structure and finite element analysis (FEA) of the induced strain in the image sensor array. (a) Schematic illustration of the panoramic artificial vision. The comb-shaped image sensor array and the g-ML array are integrated on the spherical 3D structure. **(b)** Schematic illustration defining the acceptance angle ($\Delta\theta$) and inter-ommatidial angles in the vertical and horizontal directions ($\Delta\phi_v$ and $\Delta\phi_h$). Considering the acceptance angle, the inter-ommatidial angles are determined to avoid overlapping between the visual fields of neighbouring pixels. **(c)** Geometry of the g-ML used for FEA. **(d)** Elastic modulus (e) of each layer in the g-ML. **(e)** Strain distributions induced in the image sensor and g-ML arrays. Because the outermost lens has the highest elastic modulus, the entire g-ML experiences only a nominal strain under the bending deformation.



Extended Data Fig. 6 | Imaging simulations for the optical parameters of the artificial vision. (a) Imaging simulation results of a cubic pattern with eight different acceptance angles ($\Delta\theta$) from 5.7° to 18° . The inset shows an original image of the cubic pattern. **(b)** Imaging simulation results of a cubic pattern with eight different inter-ommatidial angles ($\Delta\phi$) from 1° to 15° . The dashed boxes indicate the used conditions in the measurement.



Extended Data Fig. 7 | Optical simulations for inter-ommatidial and acceptance angles. (a) Schematic for the distance-relative visual field of the ommatidia with an acceptance angle of $\Delta\theta$ and an inter-ommatidial angle of $\Delta\phi$. (b) Illustration for the visual field variation by changing the acceptance and inter-ommatidial angles. An undetectable region, the area which cannot be captured by ommatidia, can be compensated by changing the angles. (c) Schematic illustration for describing the number of ommatidia capturing the object. (d) Calculated number of related ommatidia in (c) as a function of the acceptance angle and inter-ommatidial angle at an object distance of 5 mm, 40 mm, and 80 mm. (e) Original crab image for the image simulation. (f) Results of the imaging simulation with an object distance of 5 mm and an inter-ommatidial angle of 1°. (g) Results of the imaging simulation at an object distance of 40 mm with various acceptance angles and inter-ommatidial angles for the enhanced imaging resolution.



Extended Data Fig. 8 | Simulation and experimental results of the panoramic imaging by the artificial vision. (a) Schematic illustration of the artificial vision from the top view. **(b)** Simulation results of the panoramic imaging. **(c)** Experimental results of the panoramic imaging by the artificial vision.

Supplementary information

An amphibious artificial vision system with a panoramic visual field

In the format provided by the
authors and unedited

Supplementary Information

An amphibious artificial vision system with a panoramic visual field

Mincheol Lee^{1,2,†}, Gil Ju Lee^{3,4,†}, Hyuk Jae Jang^{3,†}, Eehyung Joh^{1,2}, Hyojin Cho^{1,2}, Min Seok Kim³, Hyun Myung Kim³, Kyeong Muk Kang³, Joong Hoon Lee³, Myungbin Kim^{1,2}, Hongwoo Jang⁵, Ji-Eun Yeo³, Frédo Durand⁶, Nanshu Lu⁷, Dae-Hyeong Kim^{1,2,8,*}, and Young Min Song^{3,*}

¹Center for Nanoparticle Research, Institute for Basic Science (IBS), Seoul 08826, Republic of Korea.

²School of Chemical and Biological Engineering, Institute of Chemical Processes, Seoul National University, Seoul 08826, Republic of Korea.

³School of Electrical Engineering and Computer Science, Gwangju Institute of Science and Technology, 123 Cheomdangwagi-ro, Buk-gu, Gwangju 61005, Republic of Korea.

⁴Department of Electronics Engineering, Pusan National University, Busandaehakro 63 beon-gil 2, Geumjeong-gu, Busan 46241, Republic of Korea.

⁵Texas Materials Institute, University of Texas at Austin, Austin, TX 78712, USA.

⁶Computer Science and Artificial Intelligence Laboratory, Massachusetts Institute of Technology, Cambridge, MA 02139, United States

⁷Center for Mechanics of Solids, Structures and Materials, Department of Aerospace Engineering and Engineering Mechanics, Department of Biomedical Engineering, Texas Materials Institute, University of Texas at Austin, Austin, TX 78712, USA.

⁸Department of Materials Science and Engineering, Seoul National University, Seoul 08826, Republic of Korea.

[†]These authors equally contributed to this work

*Correspondence to: dkim98@snu.ac.kr and ymsong@gist.ac.kr

Supplementary Notes

Supplementary Note 1. Experimental setup for the micro-lens characterization

Extended Data Figure 3 depicts the imaging demonstration setup. The micro-lens array was laminated on a slide glass, and this slide glass was fixed in a water container fabricated using a 3D printer (Ultimaker 3, Ultimaker, The Netherlands). Another slide glass was attached to the water container to secure a light path and seal water inside the container. The container was fixed on an optical rail for its facile movement. A linear motorized stage controlled the movement of the micro-lenses to investigate the variation of the focusing feature with the distance. To analyse the focal spots and lengths, lasers with three different wavelengths (450, 532, and 635 nm; CPS450, CPS 532, and CPS 635R, respectively; Thorlabs, Inc., Germany) were used. An objective lens with a magnification of $\times 10$ was placed on the micro-linear stage to capture the focal spot corresponding to each distance. An image sensor with Bayer red, green, and blue filters captured the image formed by the objective lens.

To image the object (e.g. letter 'E'), a diffuse and uniform plane light source (MB-TBL1X1-W-24CV, Vision Light Tech., The Netherlands) provided white light illumination, and a chromium-coated soda-lime glass with a desired pattern was mounted on the light source. The patterned chromium-coated glass served as a shadow mask, which generated a pattern of white light. For the facile wetting of the lens, the *h*-ML and *g*-ML were coated with silica nanoparticles to make their surface hydrophilic. The *g*-ML maintained the hydrophilic coating after several wetting/drying steps, whereas the coating layer on the *h*-ML was partially removed even after a single wetting step owing to the surface curvature (**Supplementary Fig. S20a**). The silica nanoparticles were sufficiently small (< 50 nm) so that they did not distort the incident wavefront, yielding the clear image formation (**Supplementary Fig. S20b**).

Supplementary Note 2. Ray density simulation to assess effects of the ocular shape

Commercial software (MATLAB 2018A, Mathworks, Inc., USA) was used to simulate the ray densities of different ocular structures, namely the prolate, spherical, and oblate shape, by using the following ellipsoidal equation:

$$\frac{x^2}{a^2} + \frac{y^2}{b^2} + \frac{z^2}{c^2} = 1,$$

where a , b , and c are positive real numbers utilized to determine the shape of the ellipsoid, and x , y , and z are positions on the ellipsoidal surface in the Cartesian coordinate system. a and b were defined as 10, and c was set to 1, 10, and 100 for the oblate, spherical, and prolate shapes, respectively.

To visualize the FoVs on a flat object plane, the generated ellipsoids were cut to have both azimuthal and elevation angles of 140° . As the lens parameters for compound eyes, the inter-ommatidial and acceptance angle were set to 1° and 5° , respectively. The micro-lenses were located on the ellipsoidal surfaces by satisfying the lens-related angles, and the virtual straight rays were launched from each micro-lens. The ray densities were calculated by counting the virtual rays intersecting the object plane. The maximum values of the intersection angles determined the FoVs in the horizontal and vertical directions. The object plane was positioned at a distance of 10, which is a dimensionless value, from the centre of the ellipsoidal solid.

Supplementary Note 3. Acceptance angle calculation and measurement

In the compound eye, the acceptance angle of a single ommatidium is an important parameter determining the imaging performance. The acceptance angle $\Delta\theta$ can be expressed as a following equation²,

$$\Delta\theta = \sqrt{\left(\frac{\lambda}{D}\right)^2 + \left(\frac{d}{f}\right)^2},$$

where λ/D and d/f are the angular sensitivities resulting from the diffraction at a facet lens with diameter D and the aberration related to the photodiode size d and the focal length of the micro-lens f . In our micro-lens, D is much larger than the wavelength, making λ/D negligible. Therefore, the acceptance angle was simplified to d/f . The designed micro-lens has a height of 2.27 mm from the photodiode, and the photodiode has a maximum size of 210 μm (**Supplementary Fig. S21a**). The acceptance angle was mathematically estimated to be $\sim 5.7^\circ$ based on these structural parameters.

To confirm this theoretically calculated value, we measured the photocurrent intensity of the device in a flat state by using a collimated 532 nm laser (CPS532, Thorlabs, Inc., Germany) (**Supplementary Figs. S21b and S21c**). By tilting the device with the rotation centre located at the micro-lens, we could obtain the normalized intensity as a function of the incident angle (**Supplementary Fig. S21d**). The results show that the half-maximum intensities occur at incident angles of $\pm 3^\circ$. These measurements confirm that the fabricated *g*-ML has an acceptance angle of 5.7° .

Supplementary Note 4. High-density artificial vision system in millimetre scales

To show the possibility of a high-density artificial vision system in mm scales, we developed a fabrication, integration, and packaging method described in **Supplementary Fig. S4a**. We fabricated the PDMS micro-lens array (MLA) using a concave MLA quartz template, which was transferred onto a flat PDMS substrate. After that, NOA1369 was spin-coated. We used femtosecond laser ablation for cutting the NOA/PDMS layers as a comb shape for its origami and wrapping on the sphere. The comb-shape origami pattern with *g*-MLs was transferred onto a glass substrate and rolled up on the spherical template with a diameter of 5 mm. **Supplementary Fig. S4b** shows the planar figure of the origami pattern for the spherical-shape artificial vision system, and the dark-gray region is cut by the femtosecond laser. **Supplementary Fig. S4c** displays the cross-sectional view of the proposed *g*-ML array with a pitch of 50 μm . **Supplementary Fig. S4d** illustrates the three-dimensionally rendered form of the proposed high-resolution *g*-ML array (540,504 pixels). Moreover, if the high-density photodetectors can be fabricated with an assistance from foundry companies, the artificial vision systems with a variety of configurations can be realized (**Supplementary Fig. S4e**).

Based on the proposed fabrication method, we implemented a high-density version of the artificial vision system (artificial vision system with the *g*-ML array but without photodiodes, **Supplementary Fig. S5a and S5b**). The fabricated artificial vision system has *g*-ML pixels with a total number of 540,504. A microscopy image shows a magnified view of the closely-packed *g*-MLs (**Supplementary Fig. S5c**). Because of the fabrication difficulty for the ultra-small photodiode array in the academic research laboratory, a dummy system with only the *g*-ML array is fabricated. However, the commercially available image sensor technologies can offer the fabrication of photodetectors with sub-micron pixel pitches, which can be integrated in the future.

Hence, the g -MLs integrated on ellipsoidal or spherical geometries for the bio-inspired imaging system can show the potential of the ultra-small panoramic imaging device, which is a unique difference from the commercial panoramic cameras. The commercial panoramic cameras are based on a single-chambered-eye system, which generally consists of bulky lens elements and a flat image sensor, which are difficult to be scaled down owing to the minimum volume required for the multi-lens elements.

Supplementary Note 5. Imaging demonstration using the scanning method

The imaging performance of artificial vision was demonstrated by using a customized measurement setup. Four planar diffusive light sources (MB-TBL1X1-W-24CV, Vision Light Tech., Netherlands) provided omnidirectional and uniform white light. The device was centred in a transparent water container fabricated using a 3D printer. A scanning process was employed to enhance the effective resolution, where the panoramic and amphibious device was rotated from -10° to 10° in the x direction in increments of 1° , and from -5.3° to 5.3° in the y and z directions in increments of 0.53° , respectively. To rotate the device, three motorized stages (PR-50C, Newport, USA) were perpendicularly joined, and the aluminum frames were customized to enhance mechanical stability. The motorized rotators were connected to a controller (ESP7000, Newport, USA) for their fine adjustment.

For real-time data readout, a customized data acquisition (DAQ) board, composed of an analogue-to-digital converter (ADC) and field programmable gate array (FPGA) chips on a printed circuit board (PCB), was used to acquire data from the 16×16 pixels of the photodetector array. In the previous DAQ board, 32 anodes were directly connected to the microcontroller unit (MCU), and the cathode was connected to 32 multiplexers (ADG732BSUZ, Analog Devices, USA).³ To scan the entire pixels (32×32), 1024 ($= 32 \times 32$) times of the switching are required. Therefore, the previous measurement board requires a lot of acquisition time for capturing one image. However, in our current study, to shorten the measurement time, three multiplexers supporting 12 inputs were used (ADS124S08, Texas Instruments, USA). When one anode is selected in the MCU, three multiplexers make it possible to quickly switch three cathodes.

All pixels were connected to the DAQ board through anisotropic conductive film (ACF). The DAQ board gathered the data from the device and transmitted them to the computer via the USB-

based serial communication. The FPGA processed the data with a clock speed of 16 MHz for the real-time operation. Programmable software (MATLAB R2018a, Mathworks, Inc., USA) sent command signals to control the motorized rotation stages and the DAQ board, and obtained the photocurrent information from the device. Through post-processing, the pixelated images were rendered on the spherical surface with the radius of the artificial vision.

Supplementary Note 6. Imaging simulation with ideal characteristic parameters

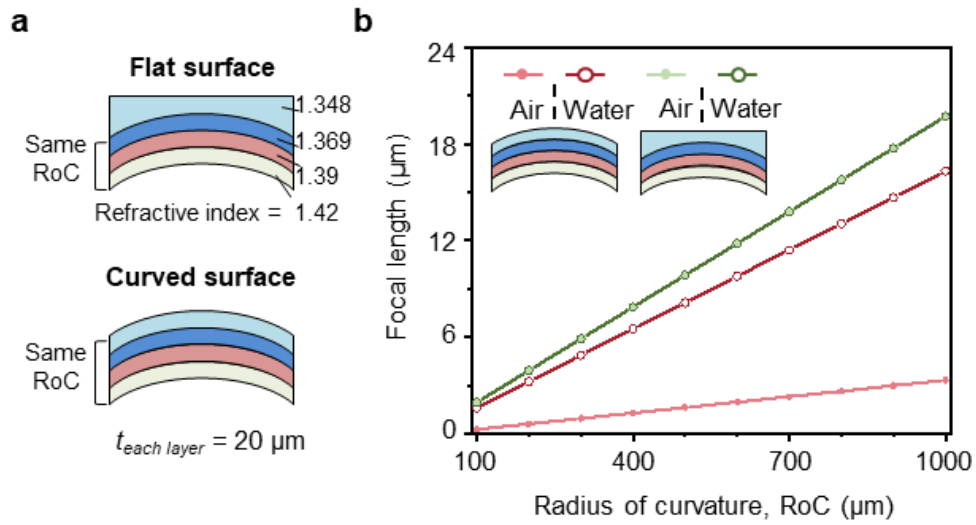
Optical simulations for the imaging by the artificial vision were performed by using commercial software (MATLAB R2018A, Mathworks, Inc., USA). The simulation mimicked the working principle of the apposition compound eye, in which the micro-optic units function individually. The simulation was performed using the ideal characteristic parameters of the artificial vision. Parallel calculations were performed to reflect the inherent parallel nature of the compound eye. The method was based on our previous report¹. An optical model was constructed, assuming that all the micro-lenses have the same optical features (i.e. same geometry and focal length) but are at different positions. Fans of ~200 randomly distributed rays were launched from the individual micro-lenses, and the propagated rays were intercepted by the detector surface. The flow chart in **Supplementary Fig. S22** illustrates the simulation process for the modeled artificial vision, which is composed of three steps¹. The first step involved building a set of single optical units, initializing the models with their ommatidium positions, inserting the object into the image ($25.4 \times 25.4 \text{ mm}^2$), and setting a scan pass for the artificial vision. In the second step, the simulation ran itself with a virtual cluster allocated for every ommatidium. The number of nodes was set equal to the number of lines for each cluster (~200). The results from each cluster included the rendered data for each ommatidium. In the final step, the sets of individually rendered data were processed into a single rendered image.

Supplementary Note 7. Comparison between the conventional panoramic system and the artificial vision system

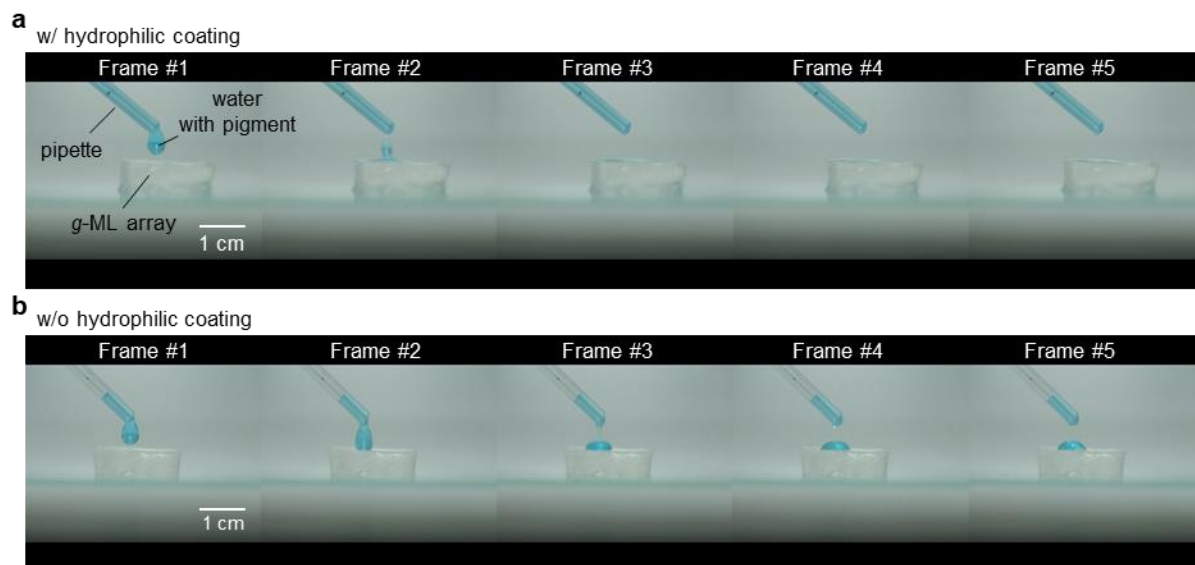
The volume of the commercial panoramic camera is difficult to be scaled down owing to the minimum volume required for the bulky multi-lens elements. However, the bio-inspired imaging system adopts the micro-lenses which are advantageous for miniaturization. From nature, we can grasp the fact that the micro-lens-based system is useful to implement the ultra-small panoramic imaging systems. For example, through the sophisticated evolution process, insects, which are representative small creatures in nature, have developed the compound eyes that feature the tiny size and the wide field of view with other exceptional imaging capabilities⁴⁻⁶.

Supplementary Fig. S9 highlights the superiority of the bio-inspired system by comparing it with the commercial panoramic camera. In the commercial panoramic camera, for example, eight conventional cameras (six cameras are for horizontal view and two cameras are facing ground and sky, which are not shown in the schematic) are merged to capture omnidirectional objects (**Supplementary Fig. S9a**). The individual camera consists of a number of lenses, and hence they require a large amount of volume. However, the bio-inspired system does not demand a large volume for the imaging optics because it adopts micro-optic units (**Supplementary Fig. S9b**). In addition, the conventional panoramic camera has blind spots at a near distance (**Supplementary Fig. S9a**). Also, the depth of field is an important parameter that indicates the range of the high-resolution region in the object domain (**Supplementary Fig. S9c**), and the bio-inspired system has a nearly-infinite depth of field because of the small size of the micro-lens. Hence, the spot radius with a few tens of micrometer is maintained (**Supplementary Fig. S9d**; red line). In contrast, the conventional camera has a larger spot radius as the object distance decreases owing to a finite depth of field (**Supplementary Fig. S9d**; black line). The

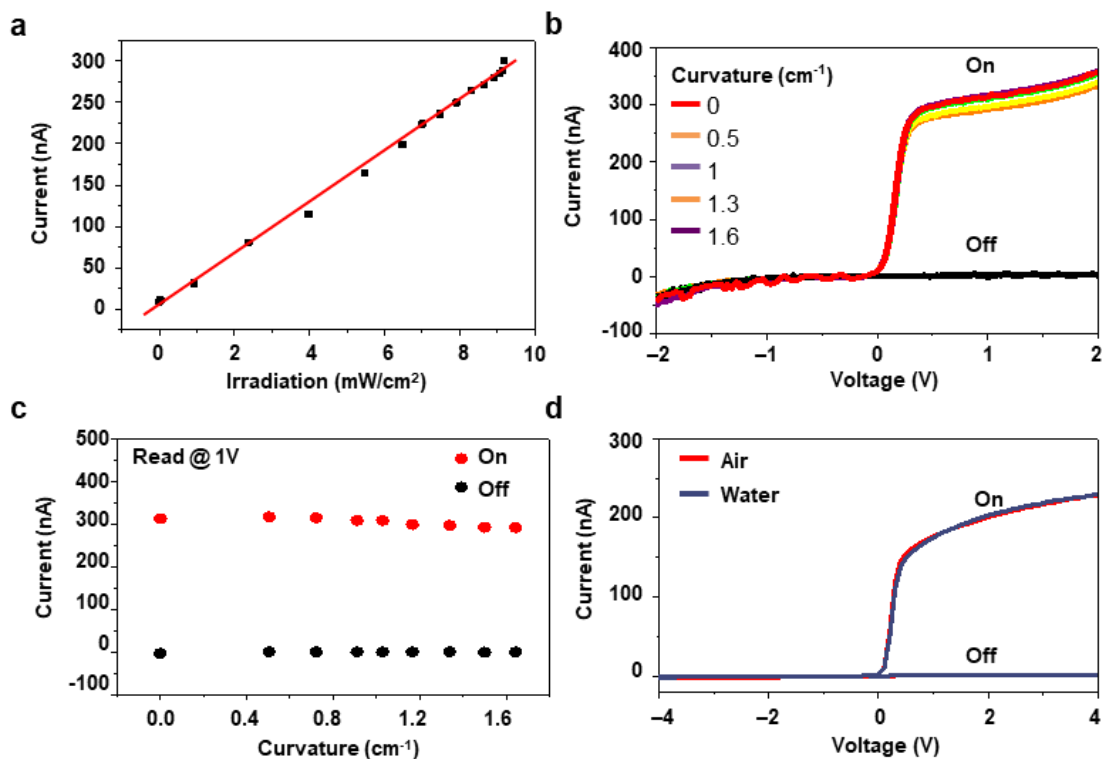
modulation transfer function (MTF) shows these dispersed focal spots by decreasing the MTF value as the object becomes closer to the imaging system (**Supplementary Fig. S9e**; black line). On the other hand, the bio-inspired system shows a constant MTF value from infinity to 10 mm. The closer the MTF value is to 1, the higher the sharpness of the imaging optical system, and the closer to 0, the lower the sharpness. In addition to imaging features, we also examine the size of imaging systems (**Supplementary Fig. S9f**). For simplicity, we compare the diagonal length of both optical systems. With the same total sensor size, the diagonal lengths of the two imaging systems differ by ~10 times in all sensor sizes. This result apparently exhibits the potential of the artificial vision system toward the ultra-small panoramic camera. However, the commercial panoramic cameras have a fundamental limitation to be smaller. Also, in the case of the smaller commercial panoramic cameras, the manufacturing difficulty of the multiple lens system will increase exponentially.



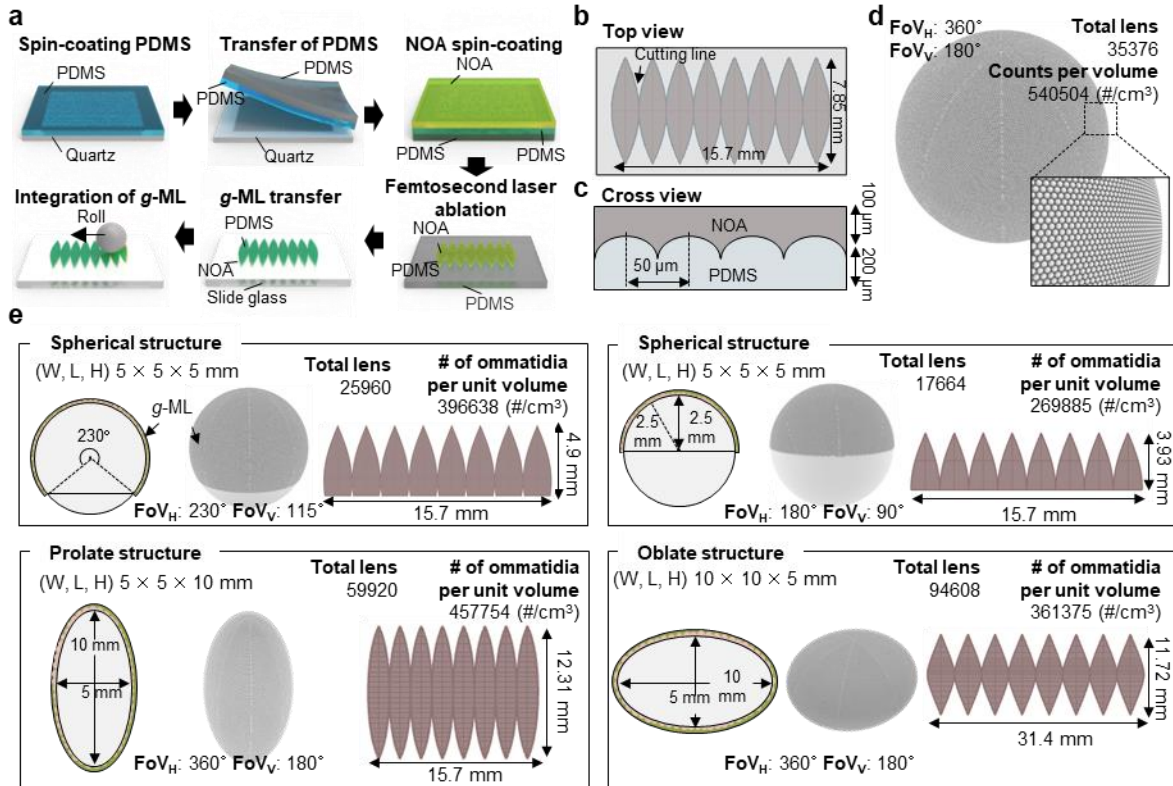
Supplementary Figure S1. Simulation results showing the role of each layer in the *g*-ML to achieve the amphibious feature and adjust the focal length. (a) Schematic illustrations for *g*-MLs with flat and curved top surfaces. (b) Focal length variation depending on the RoC of each layer. For simplicity of the simulation, the RoC and thickness for each layer are assumed to be same, respectively.



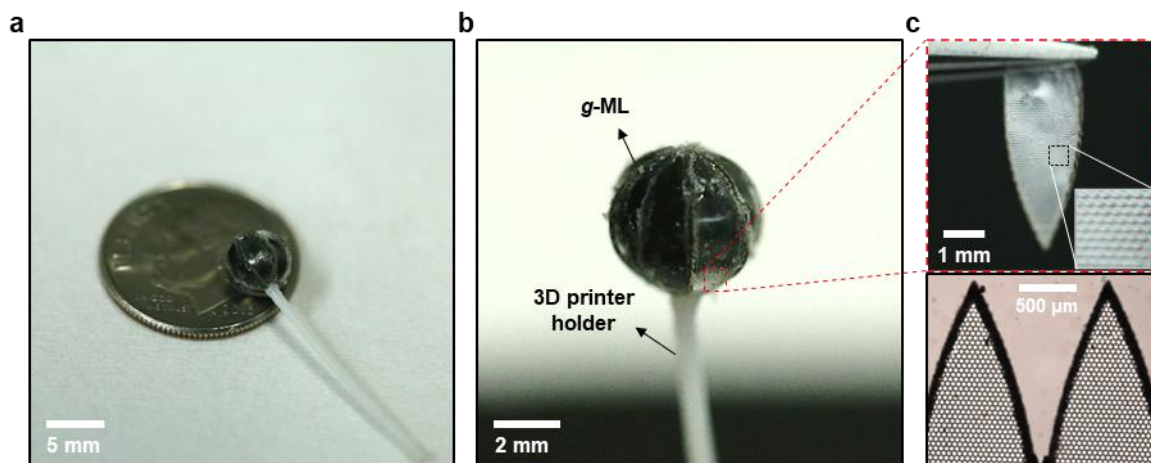
Supplementary Figure S2. Tests of the water membrane formation with and without the hydrophilic coating. Photographs of *g*-ML (a) with and (b) without the hydrophilic coating. The hydrophilic coating using silica nanoparticles instantly converts the water droplet on the *g*-ML surface into a water membrane. However, without the hydrophilic coating, the dropped water maintains the original water droplet shape.



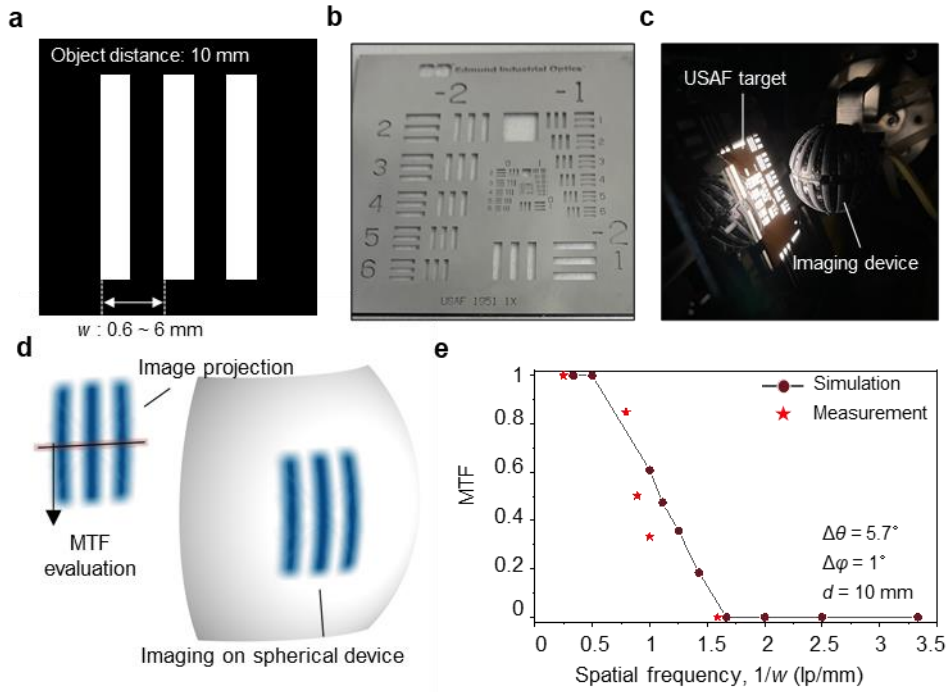
Supplementary Figure S3. Characterization of the silicon photodiode array. (a) Photo-response of a photodiode. (b) I-V curves of the photodiode under bending deformations with various curvatures with and without external illumination (i.e. on and off). (c) On-currents and off-currents of the photodiode under various bending conditions (i.e. with various curvatures). (d) I-V curves of the photodiode in air and water.



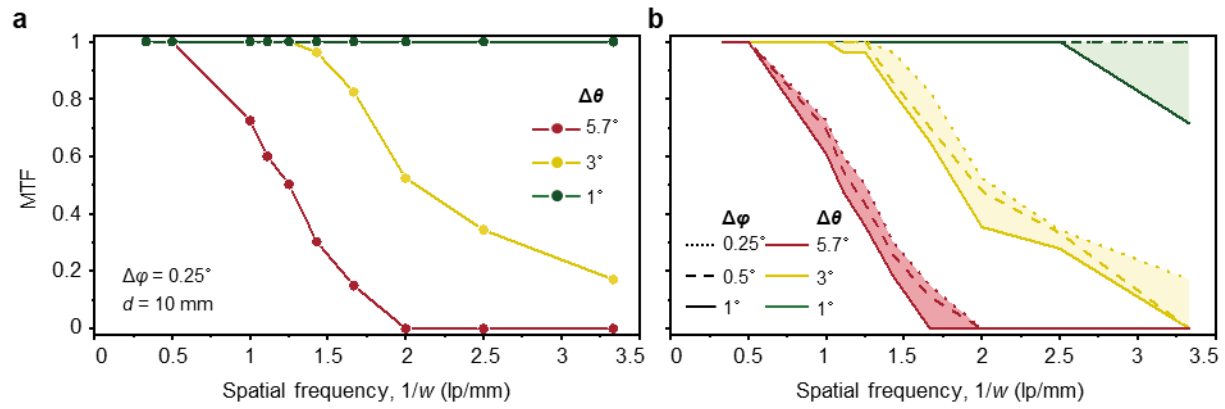
Supplementary Figure S4. Design and fabrication of origami patterns with g-MLs for artificial vision systems with various ellipsoidal and spherical structures. (a) Fabrication method of the origami pattern with g-MLs for the high-density artificial vision systems. (b) Planar figure of the origami pattern with g-MLs for the spherical-shape system. (c) Cross-sectional view of the comb-shape g-ML array. (d) Three-dimensionally rendered image and magnified view of the high-density g-ML array for the spherical-shape camera. (e) Schematics for various origami patterns and geometrical types of the compound eye-cameras using the developed packing method.



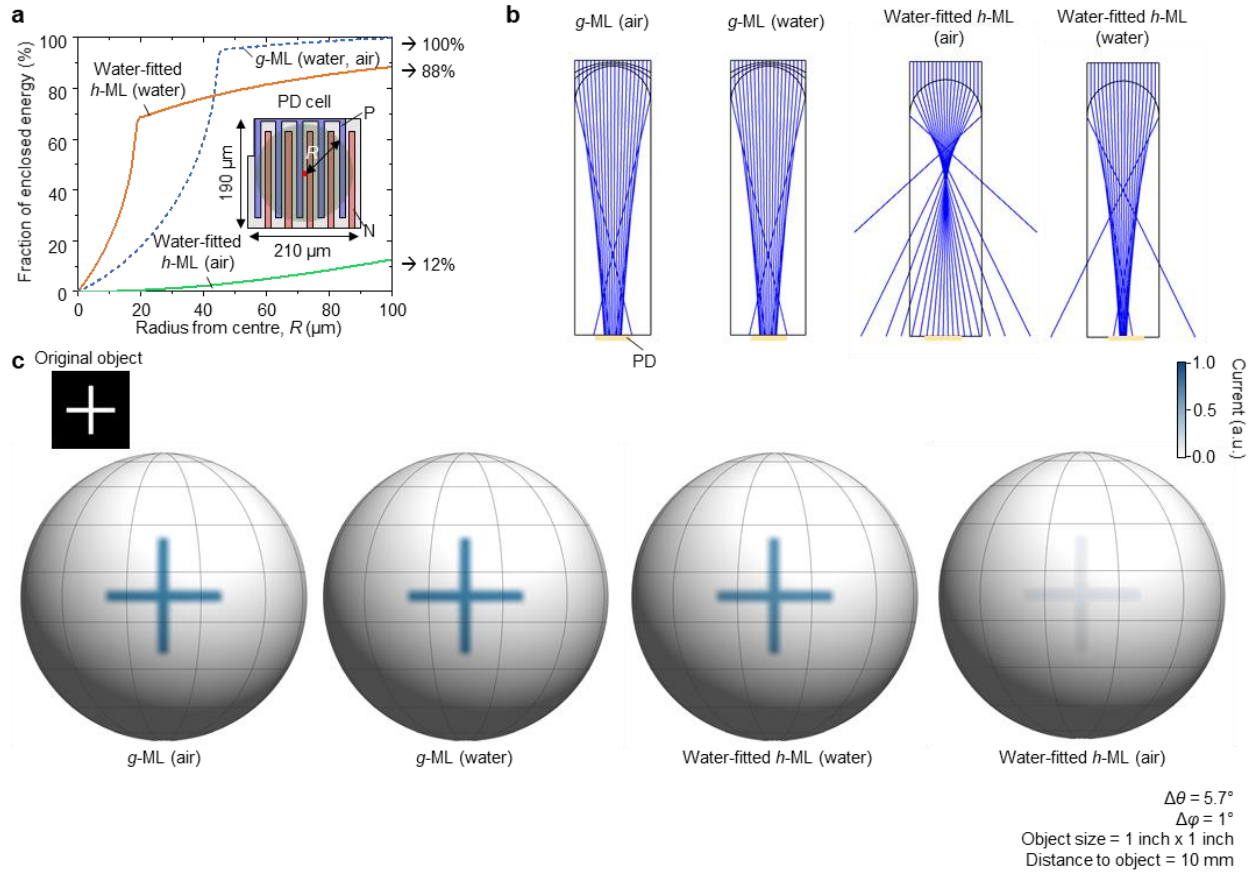
Supplementary Figure S5. Photographs of *g*-MLs integrated as a compactly-integrated array for the high-density camera. (a) Comparison of the relative size of the compactly-integrated *g*-ML array for the high-density spherical-shape system with a ten-cent coin. **(b)** Photograph of the compactly-integrated *g*-ML array for the high-density spherical-shape system. **(c)** Magnified photograph of the comb-shape *g*-ML (top) and optical microscope image for the closely-packed micro-lens array (bottom).



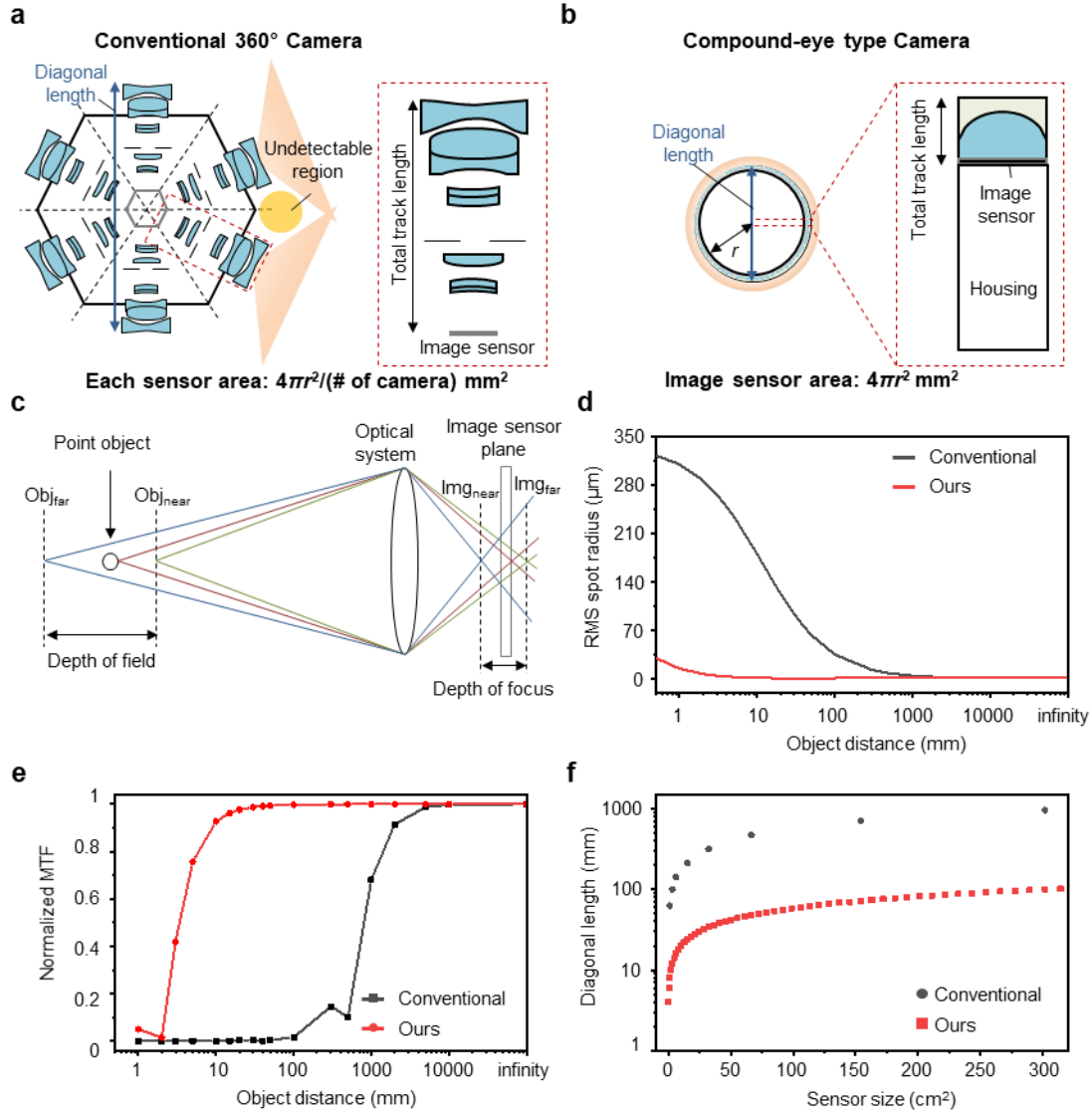
Supplementary Figure S6. Simulation and measurement of the MTF performance for the proposed device. (a) Target object used in the simulation. (b) Photograph of the USAF 1951 resolution target used in the experiment. (c) Imaging setup with the USAF 1951 resolution target and the artificial vision system. (d) Captured image by the device and projected image on the flat plane. The MTF is calculated with the line pattern on a flat plane. (e) Measured and simulated MTF graphs for the artificial vision system.



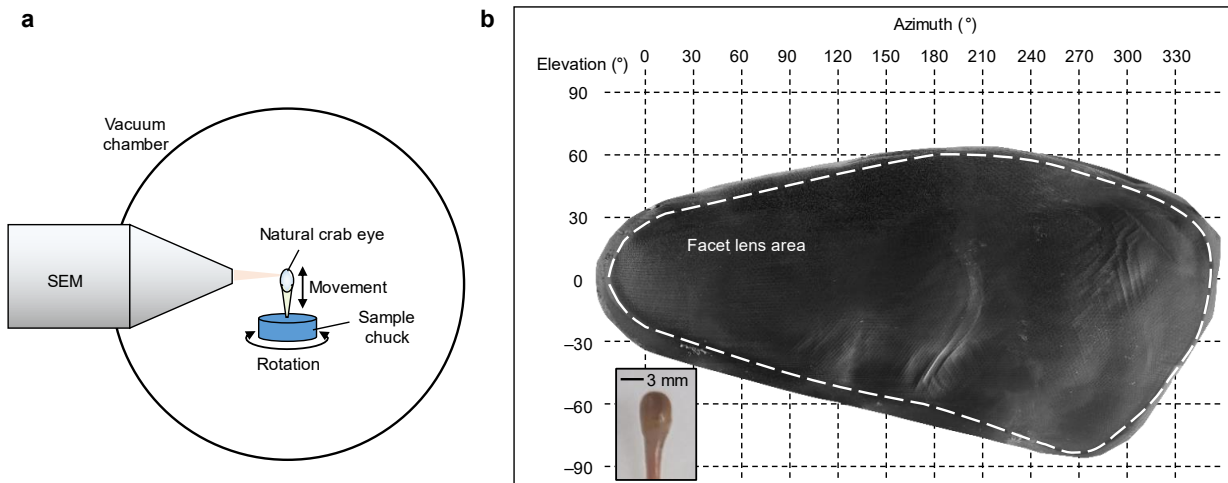
Supplementary Figure S7. Simulation of the MTF performance with various acceptance and inter-ommatidial angles. (a) The MTF graph as a function of the acceptance angle of 1°, 3°, and 5.7°. **(b)** The MTF graph as a function of various acceptance and inter-ommatidial angles.



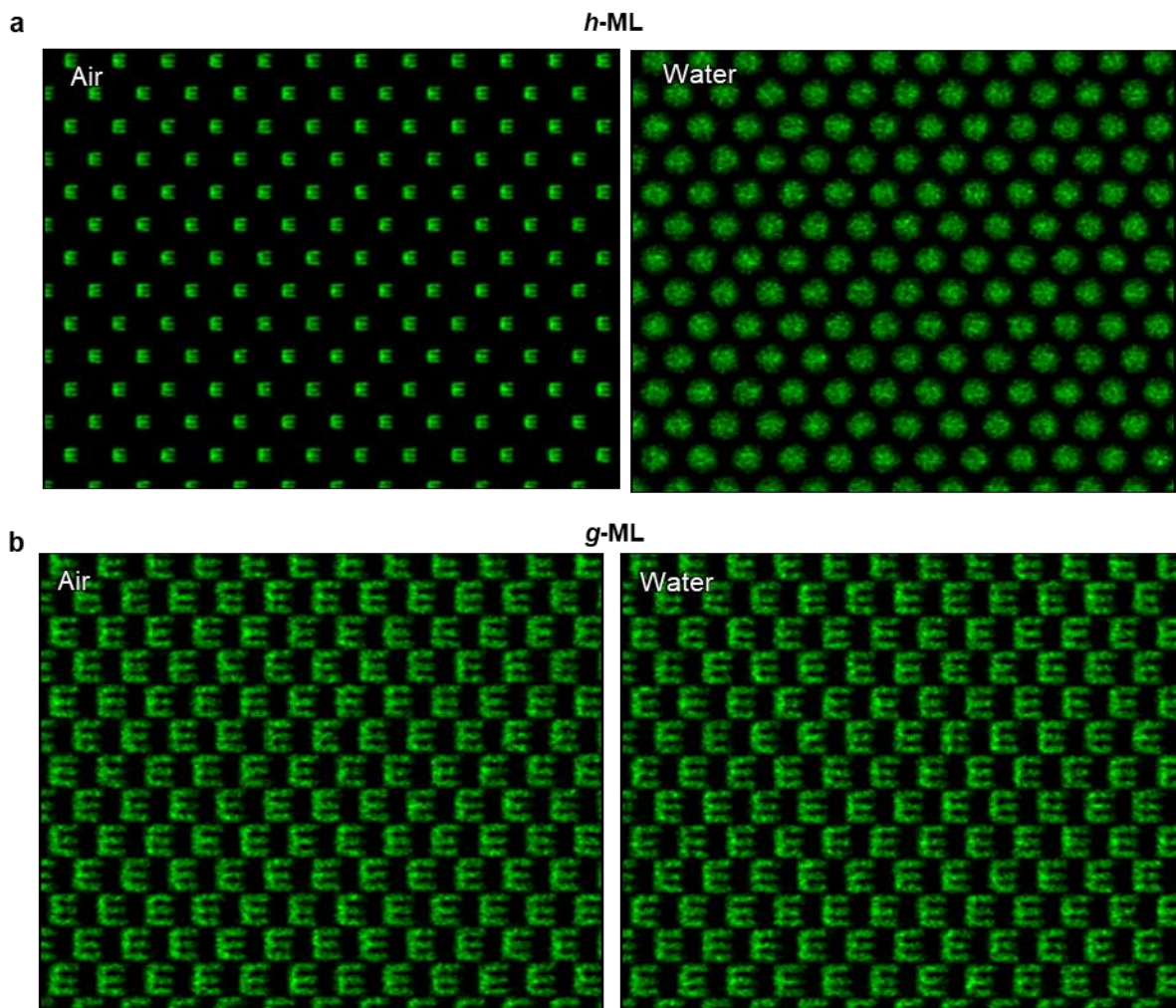
Supplementary Figure S8. Optical simulation of the light-gathering efficiency and focusing capability for the g -ML and h -ML. (a) Optical simulation for the light-collecting efficiencies of the g -ML and h -ML in air and water. The g -ML shows a light-collecting efficiency of 100% regardless of the external medium, whereas the h -ML exhibits a relatively low efficiency of 88% in water. In air, the h -ML shows an extremely low efficiency of ~12%. (b) Ray-tracing simulation results for the g -ML and h -ML in both media. The g -ML shows same results in air and water. For the h -ML in air, the refracted rays at the edge of the micro-lens do not reach the pixel, reducing the efficiency. Under water, the h -ML cannot form a focal spot on the pixel. (c) Imaging simulation results of the artificial vision for light focusing by the g -ML and h -ML in air and water. The g -ML produces a clear image of the ‘+’ symbol in both air and water. The water-fitted h -ML which is designed for focusing in water exhibits tolerable imaging results, but the results have a relatively low contrast. However, the water-fitted h -ML in air almost loses its focusing feature. Thus, the pattern is not recognizable. The original pattern and the simulation parameters are shown in the left-top and lower-right corner of the frame, respectively.



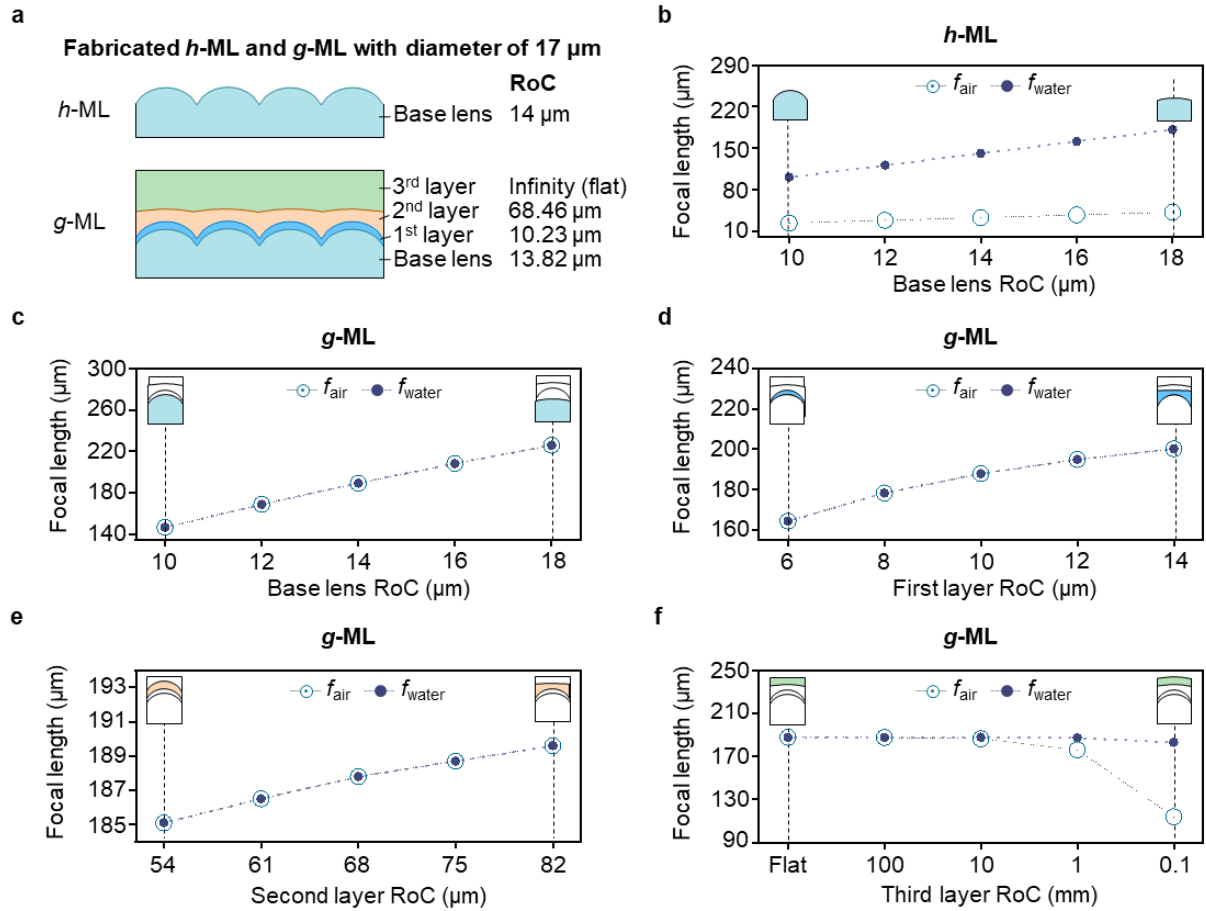
Supplementary Figure S9. Comparison between the conventional panoramic camera and the artificial vision system. (a) Schematic illustration of the conventional 360° system and (b) the artificial vision system with the same image sensor area. (c) Schematic illustration of the depth of field and depth of focus. (d) RMS spot radii for two optical systems as a function of the object distance. (e) MTF graph as a function of the object distance in the conventional 360° system and the artificial vision system. (f) Size comparison between the conventional 360° system and the artificial vision system with various sensor sizes.



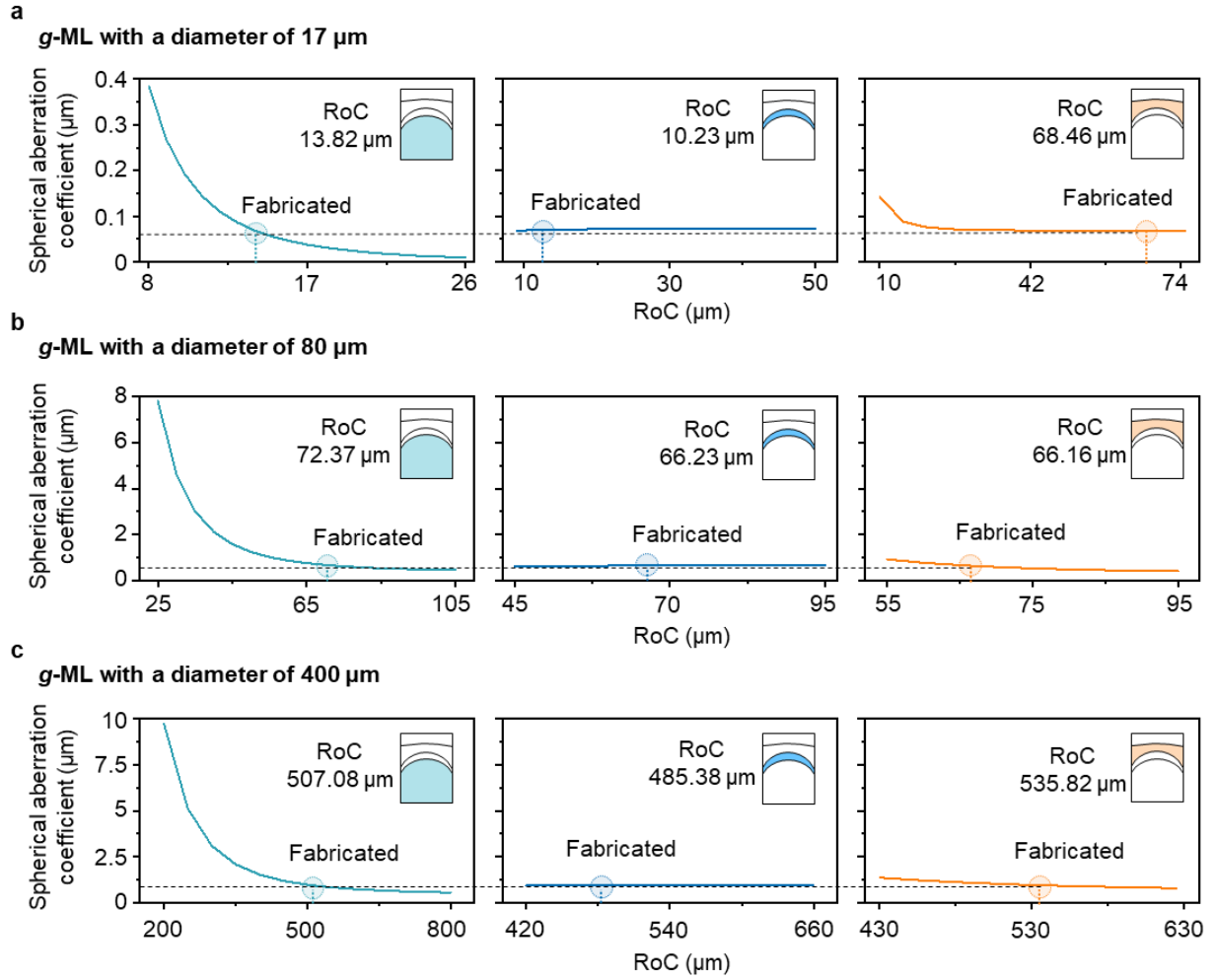
Supplementary Figure S10. Experimental setup for visual map reconstruction and reconstructed map. (a) Schematic illustration of the measurement setup using SEM. **(b)** Reconstructed SEM image of an eye of the fiddler crab in the 2D space. The inset shows an image of the eye on the rotation stage.



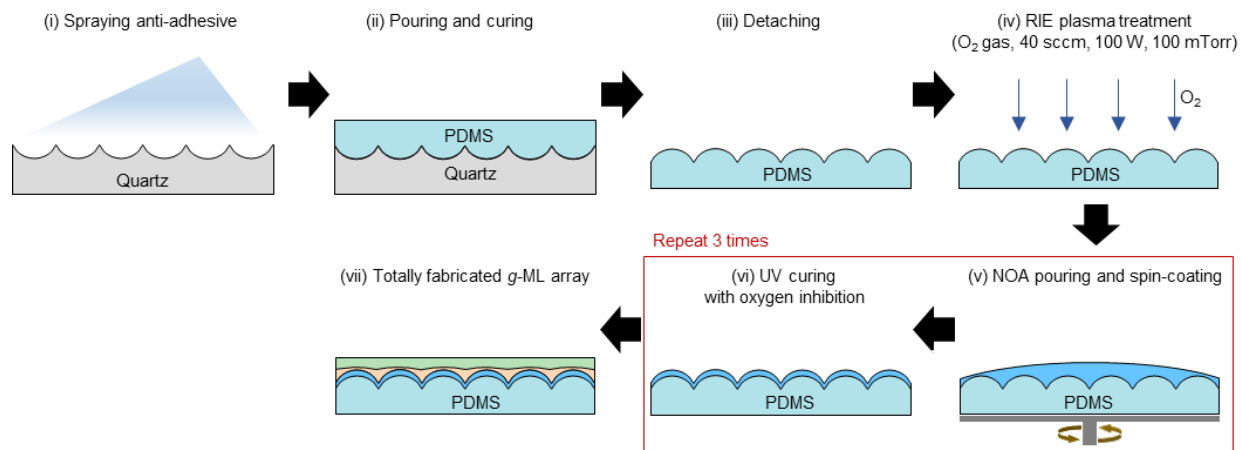
Supplementary Figure S11. Computational simulation for the focal spot formation by the h -ML and g -ML. Computational simulation results showing the differences in the focal spot formation between (a) the h -ML and (b) the g -ML in air (left) and water (right).



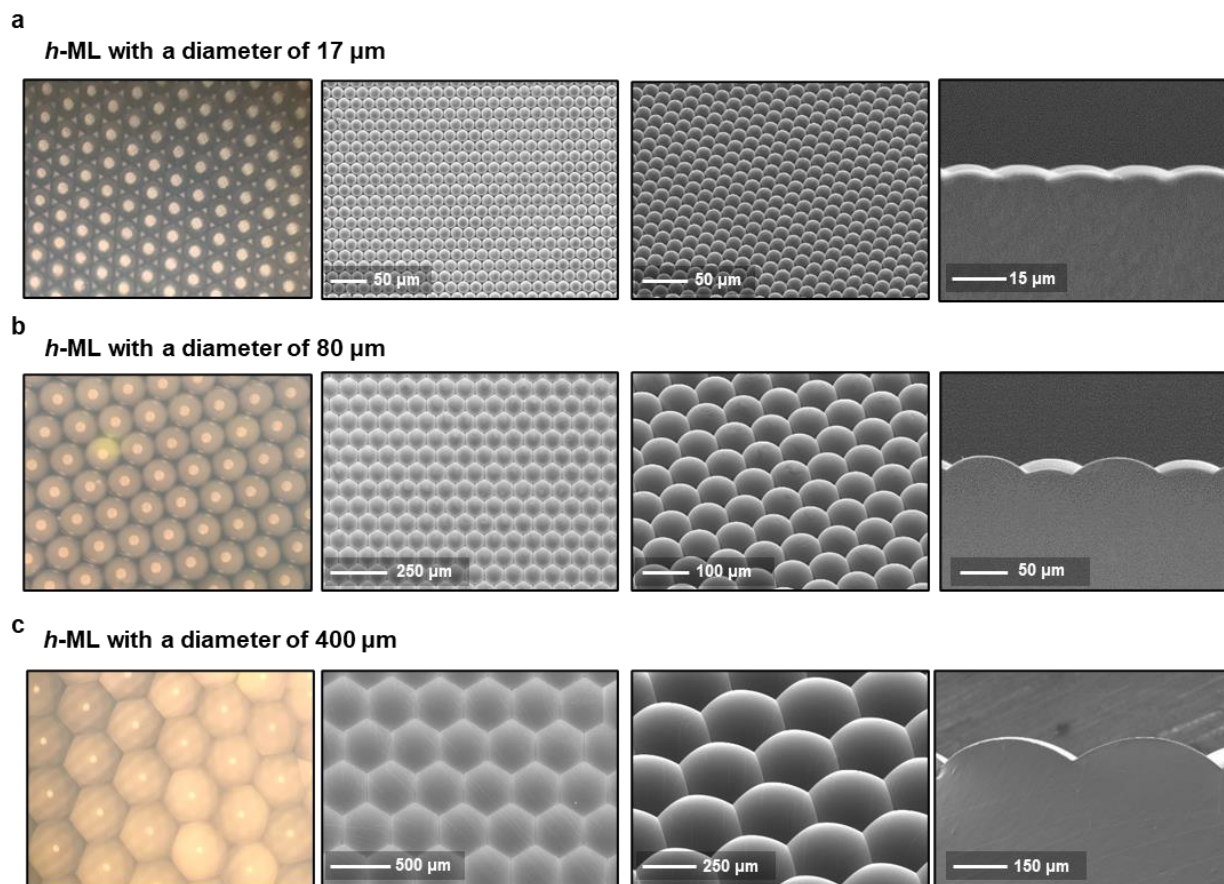
Supplementary Figure S12. Optical simulation to compare the focal lengths of micro-lenses with various RoCs in air and water. (a) Schematic illustrations of the geometries of the *h*-ML and *g*-ML (diameter: 17 μm) (left) and the RoC information for each layer of each micro-lens (right). (b–f) Calculated focal lengths in air and water (f_{air} and f_{water}) as a function of the RoC of the base lens of the *h*-ML (b), the base lens of the *g*-ML (c), the first layer of the *g*-ML (d), the second layer of *g*-ML (e), and the third layer of *g*-ML (f). The insets in (b)–(f) show the cross-sectional structures of the micro-lenses at different RoCs (noted with the vertical dashed lines). The coloured region in each cross-sectional structure corresponds to the layer whose RoC was changed in the simulation. The RoC was varied for each layer according to the RoCs shown on the x axis in (b)–(f), while the RoCs shown in (a) were used for the other layers. These results demonstrate that none of the layers except for the third layer influence the amphibious imaging and that the third layer is robust against the RoC variation (i.e. the amphibious imaging ability is maintained between the flat state and a RoC of 10 mm).



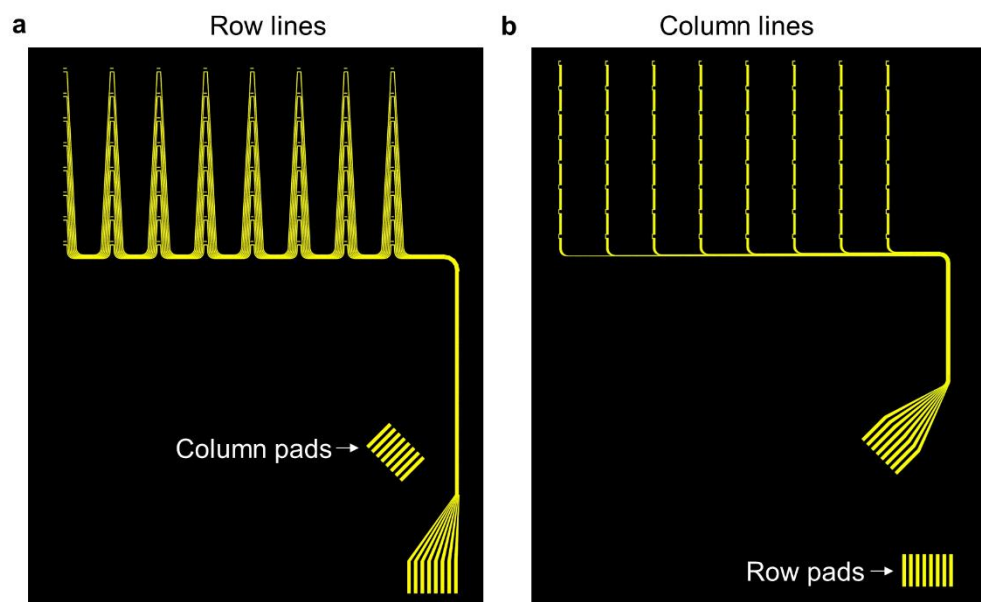
Supplementary Figure S13. Analytically calculated Seidel spherical aberration coefficients as a function of the RoC of each layer in the *g*-ML. The Seidel spherical aberration coefficients were calculated as a function of the RoC of the base lens (left), first layer (centre), and second layer (right) of the *g*-ML with a diameter of (a) 17 μm , (b) 80 μm , and (c) 400 μm , while the top (third) layer remained flat. Based on these simulation results, we designed the *g*-ML with the low spherical aberration. The insets show the specific layers (coloured layers) whose RoCs were varied in the simulation.



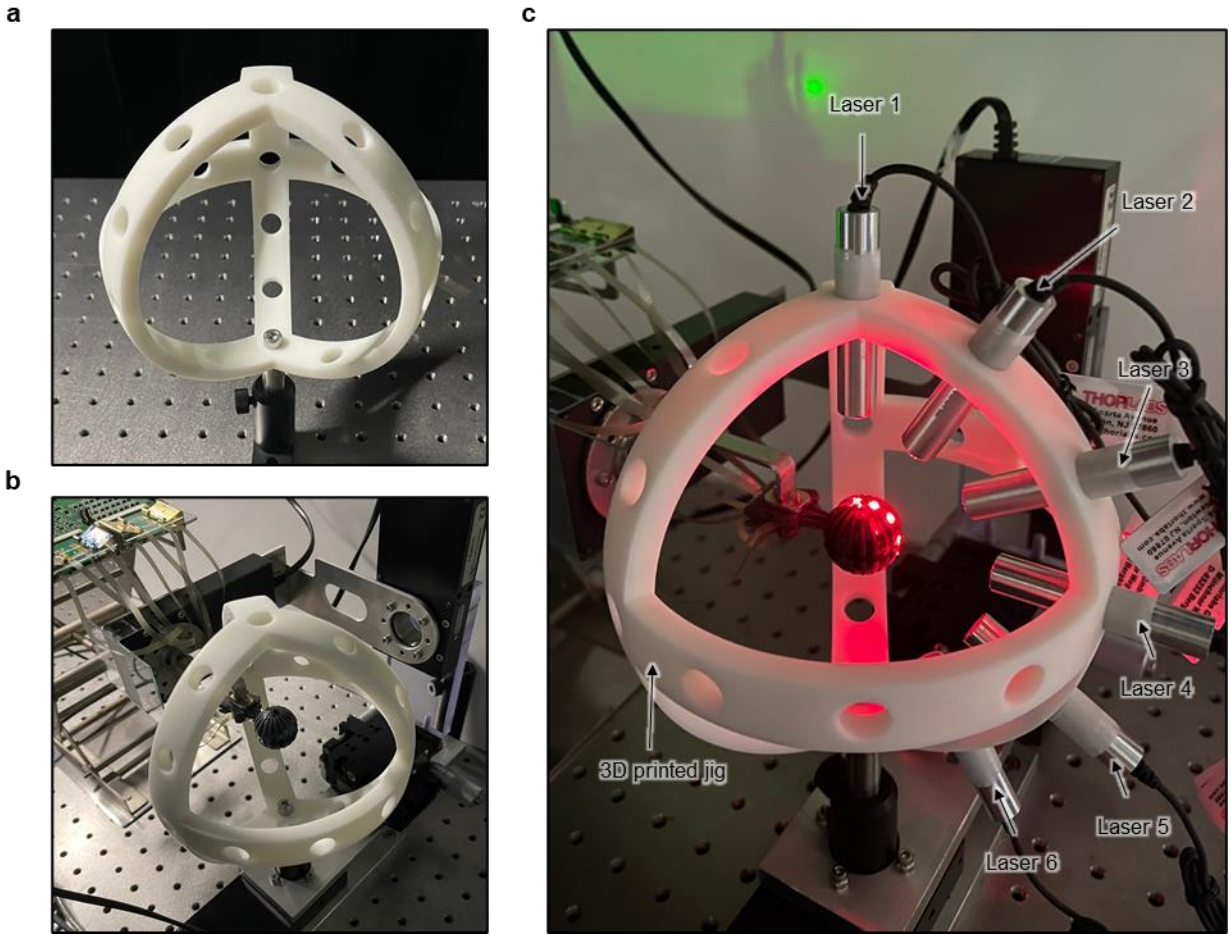
Supplementary Figure S14. Schematic illustrations for the fabrication process of the *g*-ML array which is used for the micro-lens characterization.



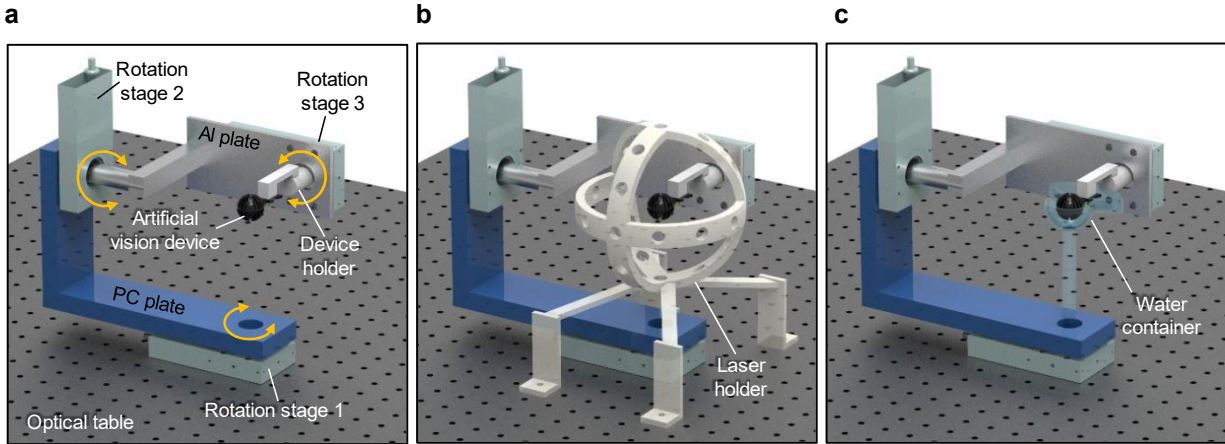
Supplementary Figure S15. SEM images of the base micro-lenses with various diameters, which are used to fabricate the *g*-ML arrays.



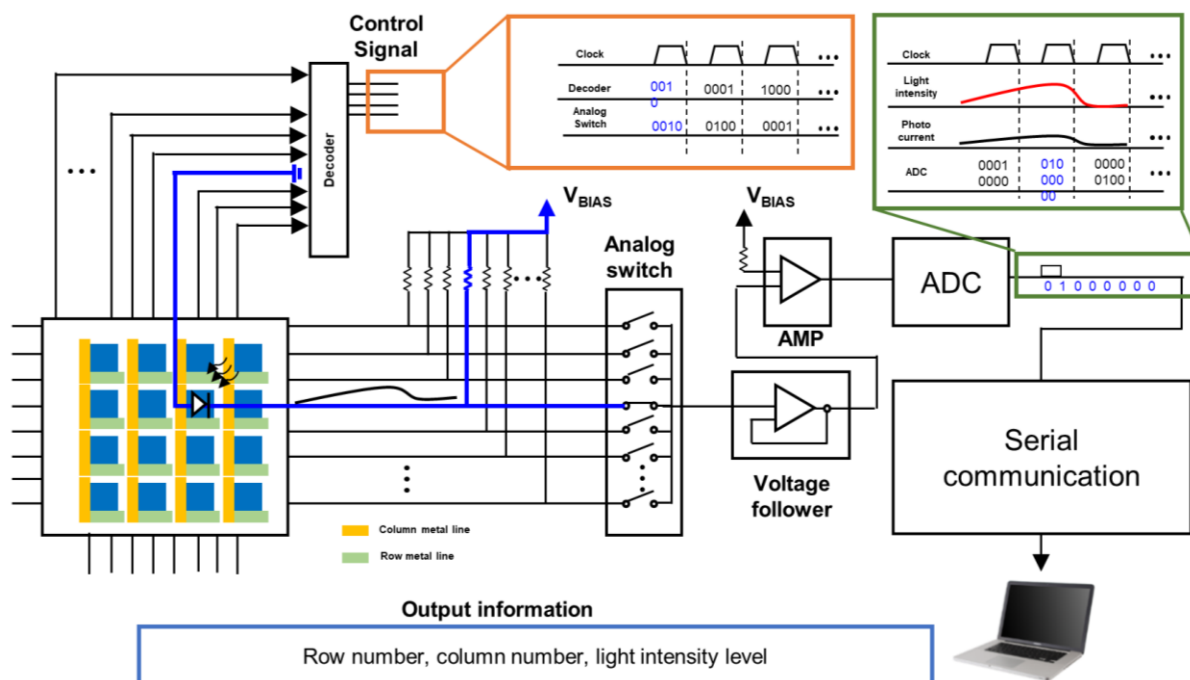
Supplementary Figure S16. Layouts of the metal interconnection layers in the comb-shaped photodiode array.



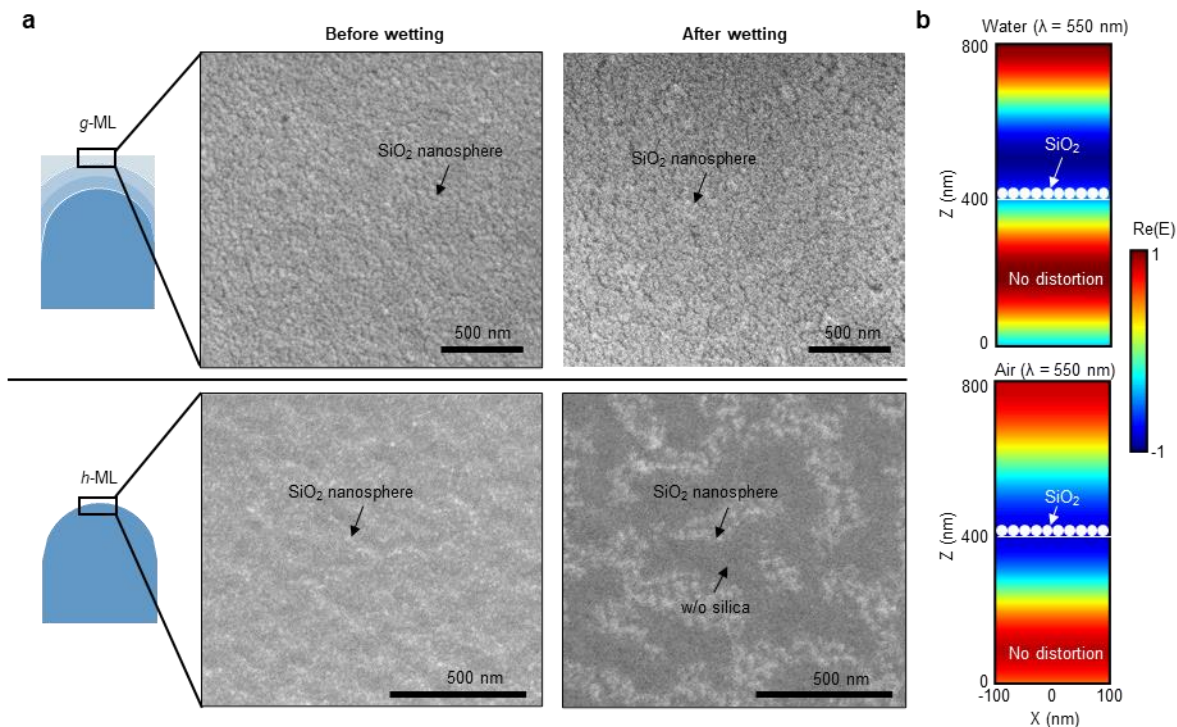
Supplementary Figure S17. Optical camera images of the custom-designed jig for the panoramic imaging demonstration by using laser illuminations.



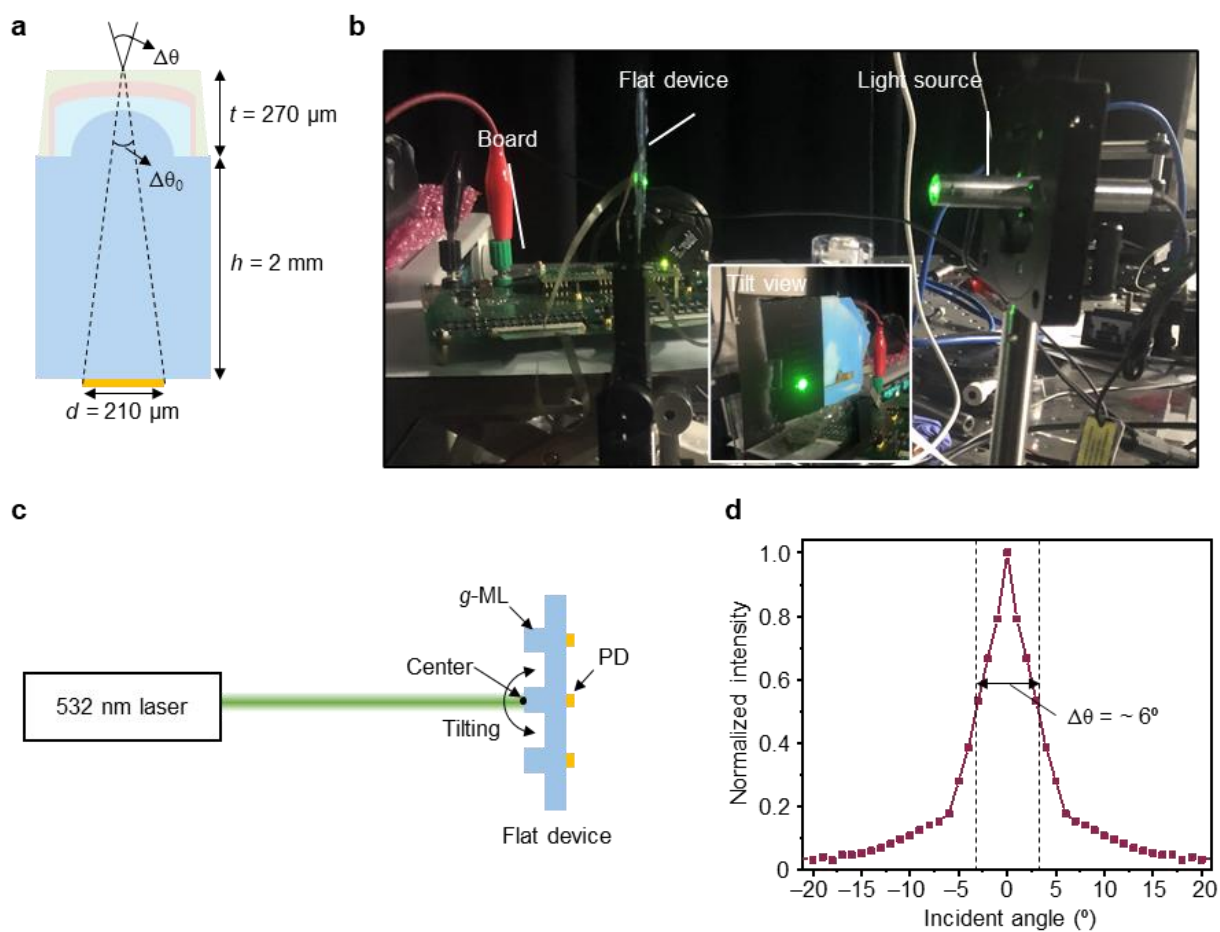
Supplementary Figure S18. Schematic illustrations of the experimental setup for the panoramic and amphibious imaging demonstration. (a) Three rotation stages are used for the scanning. (b) Panoramic imaging setup with lasers, in which the lasers are fixed by the laser holder. (c) Amphibious imaging setup using a custom-made water container. Two planar light sources with patterned masks generate object patterns, which were projected onto the artificial vision in the water container.



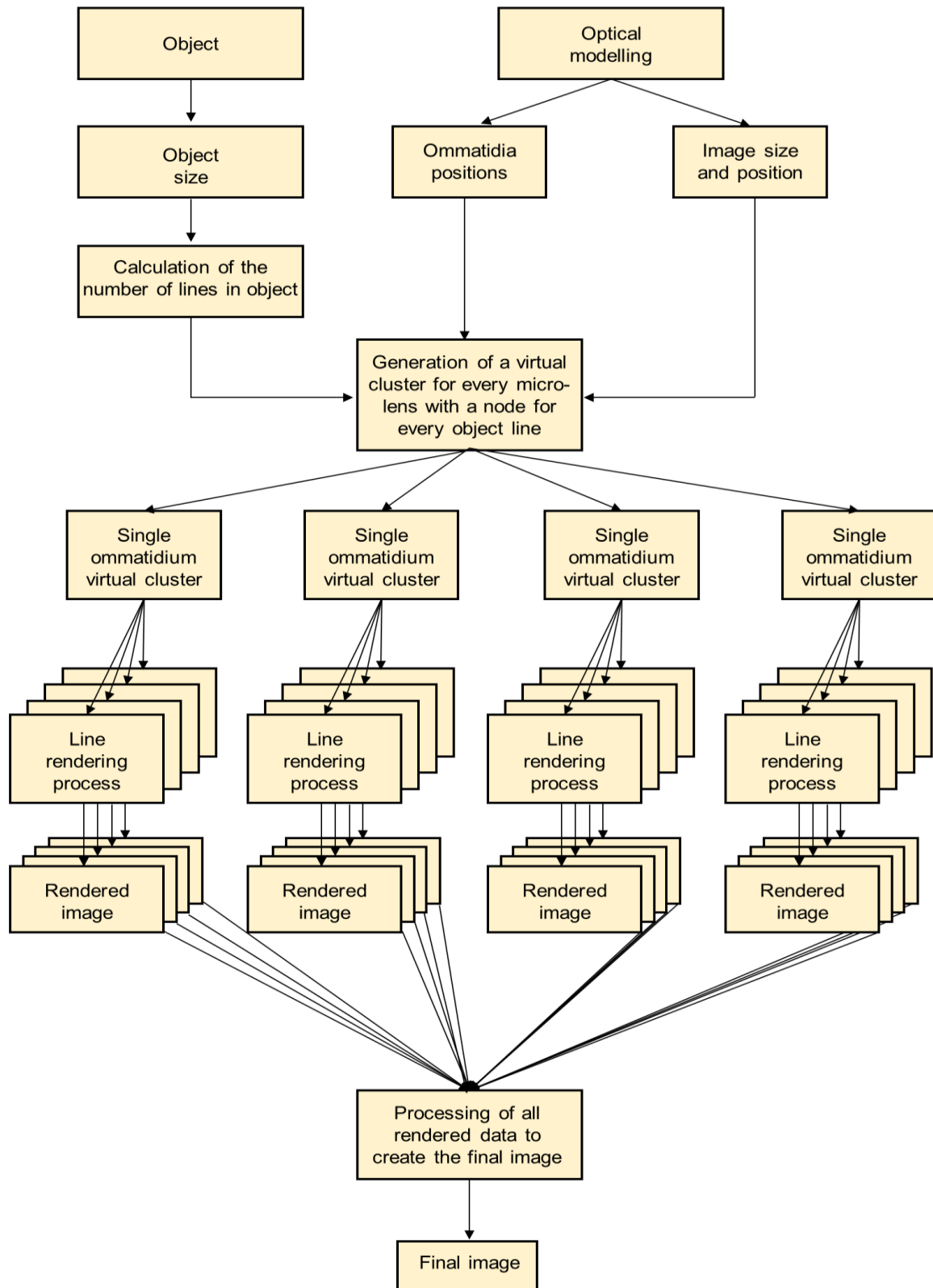
Supplementary Figure S19. Schematic diagram for the data acquisition and image processing.



Supplementary Figure S20. Surface morphology and wavefront simulations of the micro-lenses coated with silica nanoparticles. (a) SEM images of the *g*-ML surface coated with silica nanoparticles for the hydrophilic coating (top) and those of the *h*-ML surface (bottom) before (left) and after (right) wetting. In the *h*-ML, even a wetting/drying process partially removes the coated SiO₂ nanoparticles due to its curvature. However, the *g*-ML shows the same surface morphology even after repeated wetting/drying processes due to its flat surface. (b) Optical simulation results showing the effects of the wavefront distortion by the SiO₂ nanoparticles coated on the micro-lens surface. The coated SiO₂ nanoparticles do not distort the wavefront, enabling the formation of clear images.



Supplementary Figure S21. Experimental details and results for the acceptance angle of the artificial vision system. (a) Schematic illustration of the g-ML. The acceptance angle $\Delta\theta$ changes slightly due to the refractive indices of the g-ML layers. The total height of the g-ML above the PD is 2.27 mm, and the size of the PD is $210 \mu\text{m}$. (b) Photograph of the acceptance angle measurement setup. (c) Schematic illustration for the description of the measurement method. (d) Measured photocurrent intensity as a function of the incident angle of the laser beam.



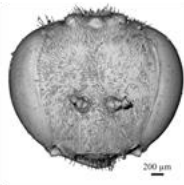



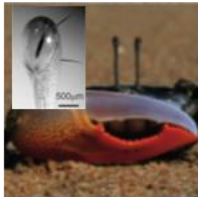
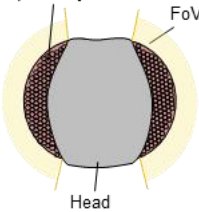
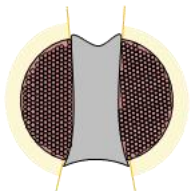
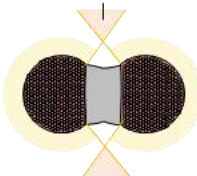
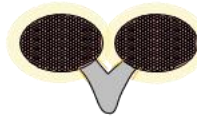
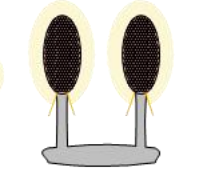




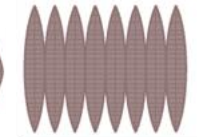
Supplementary Figure S22. Flowchart of the image simulation process.

	Habitat	Family	Species	Facet shape	Compound eye type	Reference
Supratidal	Land	Sesarmidae	<i>Geosesarma noduliferum</i> (Vampire crab)	Curved	Apposition	9, 10, 16
		Gecarcinidae	<i>Gecarcinus natalis</i> (Red land crab)	-	Apposition	9, 11, 16
Intertidal	Flat	Ocypodidae	<i>Uca arcuata</i> (Fiddler crab)	Flat (Graded index RI)	Apposition	7, 8, 9
	Rock region	Grapsidae	<i>Hemigrapsus sanguineus</i> (Shore crab)	Curved	Apposition	9, 13, 14
		Portunidae	<i>Macropipus depurator</i> (Swimming crab)	Curved	Parabolic	12, 14
		Majidae	<i>Maja capensis</i> (Spider crab)	Curved	Parabolic	12, 14
Subtidal	Ocean	Lithodidae	<i>Paralomis multispina</i> (Stone crab)	Flat	Reflecting	15
		Homolidae	<i>Paromola petterdi</i> (Altered crab)	-	Reflecting	14, 16
		Raninidae	<i>Ranina ranina</i> (Spanner crab)	Curved	Non-reflecting	14, 16

Supplementary Table S1. Classification of crab families. The habitats are categorized as the subtidal zone (aquatic environment), the intertidal zone (amphibious environment) on a rock or on a flat region, and the supratidal zone (terrestrial environment). Intriguingly, *Uca arcuata*, known as the fiddler crab in the family Ocypodidae, adopts a flat corneal facet lens with a graded RI, which is suitable for amphibious imaging, whereas other crab families have curved facet lenses, which are not ideal for an amphibious environment (c.f., the family Lithodidae has a compound eye in which the corneal facet lens is not essential for imaging, and the function of its flat cornea is different from that of Ocypodidae).

Homogeneous micro-lens (<i>h</i> -ML)				
Surface	Radius (mm)	Thickness (mm)	Material	Semi-diameter (mm)
Object	Infinity	Infinity	-	Infinity
1	Infinity	0.500	Water or Air	0.200
2	0.700	0.120	PDMS (n = 1.42)	0.200
Stop	Infinity	2.000	PDMS (n = 1.42)	0.200
Image	Infinity	-	-	0.100
Concave graded RI micro-lens (<i>g</i> -ML)				
Surface	Radius (mm)	Thickness (mm)	Material	Semi-diameter (mm)
Object	Infinity	Infinity	-	Infinity
1	Infinity	0.500	Water or Air	0.200
2	Infinity	0.010	PDMS (n = 1.42)	0.200
3	-0.250	0.010	NOA 139 (n = 1.39)	0.200
4	-0.230	0.010	NOA 1369 (n = 1.37)	0.200
5	-0.200	0.200	NOA 1348 (n = 1.35)	0.200
Stop	Infinity	2.000	NOA 1348 (n = 1.35)	0.200
Image	Infinity	-	-	0.100
Convex graded RI micro-lens				
Surface	Radius (mm)	Thickness (mm)	Material	Semi-diameter (mm)
Object	Infinity	Infinity	-	Infinity
1	Infinity	0.500	Water or Air	0.200
2	Infinity	0.010	NOA 1348 (n = 1.35)	0.200
3	0.250	0.010	NOA 1369 (n = 1.37)	0.200
4	0.230	0.010	NOA 139 (n = 1.39)	0.200
5	0.200	0.200	PDMS (n = 1.42)	0.200
Stop	Infinity	2.000	PDMS (n = 1.42)	0.200
Image	Infinity	-	-	0.100

Supplementary Table S2. Design specifications of the micro-lens arrays.

Parameter	Bee	Butterfly	Robber fly	Mantis shrimps	Fiddler crab
Eye diameter (mm)	1.1	2	1	3.3x5x9	2x2x1.17
Facet diameter (μm)	14.6	20	70-78	150	28
Interommatidial angle ($^\circ$)	3	11	0.4	0.5	1
# of ommatidia	2913	10400	700	6000	>9,000
FoV	<180	<180	>180	>180	>180
Photograph					
Eye shape	<p>Spherical</p> 	<p>Spherical</p> 	<p>Spherical</p> <p>Binocular vision</p> 	<p>Ellipsoidal</p> 	<p>Ellipsoidal</p> 
Artificial template					
Reference	17	18	19	20, 21	7, 22

Supplementary Table S3. Summary of the various shapes of the natural eyes. To mimic these diverse shapes in the artificial vision systems, a high degree of freedom, in terms of the device integration, is required.

Fabrication process for the <i>g</i> -ML with a diameter of 17 μm					
Layer	Material	Refractive index @ 589 nm	Spin-coating RPM (Repetitions)	N ₂ flow (L/min)	Curing time (min)
First layer	NOA 138	1.38	3000 (1)	5	3
Second layer	NOA 13685	1.3685	1500 (1)	5	3
Third layer	NOA 1348	1.348	8000 (1)	5	3
Fabrication process for the <i>g</i> -ML with a diameter of 80 μm					
Layer	Material	Refractive index @ 589 nm	Spin-coating RPM (Repetitions)	N ₂ flow (L/min)	Curing time (min)
First layer	NOA 138	1.38	1500 (1) / 5000 (1)	5	3
Second layer	NOA 13685	1.3685	1500 (2)	5	3
Third layer	NOA 1348	1.348	8000 (1)	5	3
Fabrication process for the <i>g</i> -ML with a diameter of 400 μm					
Layer	Material	Refractive index @ 589 nm	Spin-coating RPM (Repetitions)	N ₂ flow (L/min)	Curing time (min)
First layer	NOA 139	1.39	7000 (1)	5	5
Second layer	NOA 1369	1.369	5000 (1)	5	5
Third layer	NOA 1348	1.348	3000 (1)	5	5

Supplementary Table S4. Process conditions for the fabrication of the *g*-ML arrays used for the micro-lens characterization. The material, refractive index, spin-coating speed, and curing time used to fabricate each layer in the *g*-ML array are summarized.

Soft moulds used to fabricate the <i>g</i> -MLs for the integrated imaging device				
Layer number of <i>g</i> -ML	Radius of cylinder (mm)	Height of cylinder (mm)	Material	Curvature of convex shape (mm ⁻¹)
Third (Top)	0.250	0.300	NOA 1348	0
Second	0.225	0.200	NOA 1369	1.17
First	0.200	0.180	NOA 139	1.47

Supplementary Table S5. Design specifications of the soft moulds used to fabricate the *g*-ML array used for the imaging device.

Supplementary Reference

1. D.-E. Nilsson, Three unexpected cases of refracting superposition eyes in crustaceans. *J. Comp. Physiol. A*, **167**, 71-78 (1990).
2. Song, Y. M. *et al.* Digital cameras with designs inspired by the arthropod eye. *Nature* **497**, 95–99 (2013).
3. Kim, M. S. *et al.* An aquatic-vision-inspired camera based on a monocentric lens and a silicon nanorod photodiode array. *Nat. Electron.* **3**, 546–553 (2020).
4. M. F. Land, D. Nilsson, *Animal Eyes*, Oxford University Press, Oxford, UK 2012
5. J. Zeil *et al.*, The visual ecology of fiddler crabs. *J. Comp. Physiol. A* **192**, 1-25 (2006).
6. M. F. Land, The optics of animal eyes. *Contemp. Phys.* **29**, 435 (1988).
7. A. Alkaladi, J. Zeil, Functional anatomy of the fiddler crab compound eye (*Uca vomeris*: Ocypodidae, Brachyura, Decapoda). *J. Comp. Neurol.* **522**, 1264–1283 (2014).
8. J. Zeil, J. M. Hemmi, P. R. Y. Backwell, Fiddler crabs. *Curr. Biol.* **16**, R40–R41 (2006).
9. P. Castro, P. J. F. Davie, D. Guinot, F. R. Schram, J. C. von Vaupel Klein, *The Crustacea*. in *Treatise on Zoology – Anatomy, Taxonomy, Biology*, Volume 9, part C (Brill, 2015).
10. P. K. L. Ng, C. D. Schubart, C. Lukhaup, New species of “vampire crabs” (*Geosesarma de man*, 1892) from central Java, Indonesia, and the identity of *sesarma* (*Geosesarma*) *nodulifera* De Man, 1892 (Crustacea, Brachyura, Thoracotremata, Sesarmidae). *Raffles Bull. Zool.* **63**, 3–13 (2015).
11. P. T. Green, Field observations of moulting and moult increment in the red land crab, *Gecarcoidea natalis* (Brachyura, Gecarcinidae), on Christmas Island (Indian Ocean). *Crustaceana* **77**, 125–128 (2004).

12. D. E. Nilsson, A new type of imaging optics in compound eyes. *Nature* 332, 76–78 (1988).
13. K. Arikawa, K. Kawamata, T. Suzuki, E. Eguchi, Daily changes of structure, function and rhodopsin content in the compound eye of the crab *Hemigrapsus sanguineus*. *J. Comp. Physiol. A* **161**, 161–174 (1987).
14. C. L. McLay, Brachyura and crab-like anomura of New Zealand. *Leigh Laboratory Bull.* **22** (1988).
15. E. Eguchi, M. Dezawa, V. B. Meyer-Rochow, Compound eye fine structure in *Paralomis multispina* Benedict, an anomuran half-crab from 1200 m depth (Crustacea; Decapoda; Anomura). *Biol. Bull.* **192**, 300–308 (1997).
16. J. Luque, W. T. Allison, H. Bracken-Grissom, K. M. Jenkins, R. Palmer, M. L. Porter, J. M. Wolfe, Evolution of crab eye structures and the utility of ommatidia morphology in resolving phylogeny. *bioRxiv* (2019), doi:10.1101/786087.
17. Jezeera, M.A., Tichit, P., Balamurali, G.S. et al. Spatial resolution and sensitivity of the eyes of the stingless bee. *Tetragonula iridipennis*. *J Comp Physiol A* (2021), doi:10.1007/s00359-021-01521-2.
18. Lee, Ken C., Qi Yu, Uwe Erb, Mesostucture of ordered corneal nano-nipple arrays: The role of 5–7 coordination defects. *Sci Rep.* **6**, 1-11 (2016).
19. Wardill, Trevor J., et al. A novel interception strategy in a miniature robber fly with extreme visual acuity. *Curr. Biol.* **27**, 854-859 (2017).
20. Marshall, N. J., M. F. Land, Some optical features of the eyes of stomatopods. *J. Comp. Physiol. A* **173**, 583-594 (1993).

21. Marshall, N. J., M. F. Land, T. W. Cronin, Shrimps that pay attention: saccadic eye movements in stomatopod crustaceans. *Philos. Trans. R. Soc. B-Biol. Sci.* **369**, 20130042 (2014).
22. Land, Michael, and John Layne, The visual control of behaviour in fiddler crabs. *J. Comp. Physiol. A* **177**, 91-103 (1995).